



Report on Deliverable

Version 7/2/2019	Report on Water Jet Drilling Modelling	page 1/49
------------------	--	-----------

Project	H2020 - SURE (Grant-Number 654662)
Deliverable	D7.1 - Report on Water Jet Drilling Modelling
Work package	WP7 - Integration
Lead author	Jiansheng Xiang
Contributor(s)	Bin Chen, John-Paul Latham, Ado Farsi
Dissemination level	PU (public)
Type	R (document, report)
Due date	2019-02-28
Actual submission date	2019-07-02
Resubmission date(s)	
Change History	

Licence information	Report D7.1 of the Consortium of the H2020 SURE Project This publication is licensed under a Creative Commons License, International Attribution 4.0: CC BY
DOI (Repository)	10.2312/GFZ.4.8.2019.011
Recommended Citation	Xiang, J., Chen, B., Latham, J.-P., Farsi, A.; The Horizon 2020 Project SURE: Deliverable 7.1 - Report on Water Jet Drilling Modelling, 2019, Potsdam: GFZ German Research Centre for Geosciences, DOI: https://doi.org/10.2312/GFZ.4.8.2019.011



The SURE project has received funding from the European Union's Horizon 2020 research and innovation programme under grant agreement No 654662.

Table of Contents

Abbreviation list	3
1 Executive Summary	4
2 Background.....	5
2.1 Numerical simulation of water jet drilling	5
2.2 Reconstruction of rock microscale model.....	10
3 Mesoscale simulation of water jet drilling	11
3.1 Immersed Body Method (IBM) for water jet drilling	11
3.1.1 Equations for solid dynamics	12
3.1.2 Equations for fluid dynamics	12
3.1.3 Fracture model.....	13
3.1.4 Pore pressure	14
3.2 Numerical simulation setup and material properties.....	14
3.3 Boundary conditions	16
3.4 Results and discussions	16
3.4.1 Mesh adaptivity	16
3.4.2 Effect of rock strength	17
3.4.3 Failure mechanism analysis.....	18
3.4.4 Effect of pore pressure and “water back pressure”	20
3.5 Conclusions	23
4 Microscale simulation of water jet drilling	23
4.1 Re-construction of microscale model for igneous and porous sedimentary rock	23
4.1.1 Re-construction of microscale model for granite with stochastic reconstruction method.....	23
4.1.2 Re-construction of microscale model for sandstone with CT-scan data	24
4.2 FDEM-GBM model for mechanical simulation of microstructure.....	26
4.2.1 Concept of the FDEM-GBM model	26
4.2.2 Calibration of the numerical parameters	27
4.2.3 Model validation with experimental Brazilian test	32
4.3 Numerical simulation of water jet drilling including rock microstructure.....	35
4.3.1 Numerical simulation setup and material properties	35
4.3.2 Boundary conditions.....	37
4.3.3 Results and discussions	37
5 Conclusions	44
6 Acknowledgements.....	45
7 References	46



The SURE project has received funding from the European Union’s Horizon 2020 research and innovation programme under grant agreement No 654662.

Report on Deliverable

Version 7/2/2019

Report on Water Jet Drilling Modelling

page 3/49

Abbreviation list

RJD	Radial Jet Drilling
FDEM	Combined Finite-Discrete Element Method
GBM	Grain-based model
IBM	Immersed Body Method
ROP	Rate of Penetration
FEM	Finite Element Method
SPH	Smoothed Particle Hydrodynamics
CFD	Computational Fluid Dynamics



The SURE project has received funding from the European Union's Horizon 2020 research and innovation programme under grant agreement No 654662.

1 Executive Summary

The aim of this research is to investigate the failure mechanism for different types of rock in the context of water jet drilling and to predict the jet-ability or assess the radial jet drilling (RJD) performance prior to drilling and at the well petrophysical analysis stage. The main approach is to numerically simulate the water jet drilling for different types of rock using ICL's in-house fluid-solid coupling codes. The rock properties, CT-scan data and jetting results obtained from D4.1 (Bakker et al., 2018) and D5.1 (Hahn et al., 2017) provide a good foundation for the related numerical results.

The RJD performance is affected by various factors including rock properties, in-situ stress, jet velocity, etc. It is of great benefit to predict the drilling performance prior to drilling to avoid unnecessary cost. However, the failure mechanism of water jet drilling for different types of rock is still speculative and the existing numerical techniques cannot meet the need to determine these mechanisms. In this report, water jet drilling is simulated using a recently developed fluid-solid coupling approach. First, we consider the rock properties to be homogeneous and we apply what is termed a 'mesoscale' model as described in Section 3. Then in Section 4, the rock microstructure is considered to investigate the heterogeneous pore and grain-scale response to the jet, and the coupled jetting model is termed the 'microscale' model. Here, we observe microstructural mechanisms firstly for solids-only failure and then of failure due to water jet drilling.

In the mesoscale model, a new 3D immersed body method in which the fracture model was incorporated into a two-way fluid-solid coupling model is proposed. To investigate the effect of the pore water pressure, Biot's theory was implemented. The new fluid-solid coupling model together with a 3D fracture model is capable of simulating crack initiation, propagation and fragment removal under the impact load of a high-speed water jet, but for this mesoscale model, the pore space topology is not modelled explicitly. The effect of material mechanical strengths and the in-situ stress on the water jet drilling performance is investigated.

Rock failure is normally simulated with a damage or fracture model based on laboratory scale intact strength parameters. These parameters describe the rock properties sufficiently well for mesoscale or macroscale problems governed by intact rock strength but may be inadequate for specific failure mechanism, such as water jet drilling where the microstructure is believed to play an important role. In order to investigate the complex failure mechanism of sandstone in the context of water jet drilling, a microstructure model of the sandstone was constructed based on CT-scan data. A novel CT-scan based approach is proposed to mimic sandstone microstructure where pore topology is addressed in the numerical representation of the microstructure. A compromise between the accuracy of the microstructure model and the computation cost is reached. The rock's microstructural response is solved with the FDEM-GBM model by applying different properties on the inter-grain and intra-grain element boundaries. The capacity of the proposed model to simulate grain-scale failure of sandstone is demonstrated to be excellent for the solids-only case of the microscale simulation of the Brazilian disc test. The microscale simulation of water jet drilling is carried out using the same method as in the mesoscale model but considering the rock microstructure heterogeneity and pore topology. Conclusions from the modelling are as follows:



The SURE project has received funding from the European Union's Horizon 2020 research and innovation programme under grant agreement No 654662.

- According to the mesoscale modelling, under the condition of water exiting a 2 mm orifice with an average velocity of 160 m/s and standoff distance 6 mm, and atmospheric conditions, Gildehaus sandstone can be cracked and eroded under water jet impact while Dortmund sandstone, and Icelandic Basalt are harder to be eroded, which qualitatively agrees with experimental observations (see D5.1, Hahn et al., 2017). For Gildehaus sandstone, the main jet drilling rock breakdown mechanism is identified as a “water hammer effect”. The numerical results show most of the cracks are tensile failure. It is found that after considering pore pressure transient changes due to the jet pulse arriving, RJD generates cracks over a slightly wider area beneath and to the side of the jet than when pore pressure in the rock is assumed constant during jetting. When the back pressure (initial water pressure acting on rock prior to jetting) is increased from 0.1 MPa to 2.5 MPa under the same in-situ stress constraint conditions (a 5 MPa radial stress applied on side wall surfaces of a cylindrical domain), the cracking and jet penetration of rock is significantly reduced as the increased back pressure acts like an increased axial confining pressure.
- The microscale simulation of the Brazilian test for Sandstone shows the mesoscale fracture normally forms due to the breakage of the inter-grain joints, which agrees with the experimental results very well.
- The microscale simulation of water jet drilling demonstrates two jet drilling rock breakdown and erosion mechanisms: (a) water hammer tensile stress effect suggesting shock waves (elevated stress levels) for breaking apart weak inter-grain joints; (b) water-driven bursting effect suggesting water driven entry inside the pores between grains leading to bursting the grain cementation/bonding surrounding the pores. The numerical results show that a lowering of the inter-grain tensile strength and cohesion while leaving the intra-grain strengths unchanged enhances the jet-ability, as would be expected. The particular case of in-situ stress confinement and a far-field high stress ratio of 3:1 normal to the jetting direction in a true-triaxial (30:10:10 MPa) jetting test on a 300 mm cube block was considered. The simulation showed this confined loading configuration decreases the jet-ability significantly when compared with the unconfined jetting conditions also simulated.

2 Background

2.1 Numerical simulation of water jet drilling

The water jet drilling technology was first introduced in the 1960s and the initial applications were limited to cleaning and unblocking drains (Kamel, 2017). Over the past 20 years, RJD has been developed as a well stimulation technique which can enhance oil recovery. It can be used on existing wells to stimulate further extraction. RJD uses high-pressure water which is pumped through a high-pressure hose and a nozzle to drill into the rock. It erodes the rock by pumping a relatively small amount of water at high pressure and high velocity through very small orifices of the nozzle forming water jets that interact with the rock.

Recently, the RJD technology has been considered as a stimulation technique for improving low performing geothermal wells. It is reported that a low performing geothermal well in Klaipeda, Lithuania in Europe, was further stimulated by adding 12 laterals using RJD technology with lengths of up to 40 m each, leading to an increase of flows and heat to the production well and an injectivity of about 14% (Reinsch et al. 2018).



The SURE project has received funding from the European Union's Horizon 2020 research and innovation programme under grant agreement No 654662.

RJD has been claimed to be a less cost, more environmentally friendly alternative to hydraulic fracturing. However, there are some challenges and limitations to this technology. One of them is that at present it cannot be used in all situations, e.g. RJD with a static nozzle is able to drill into sandstone, but water jet penetration into hard rock, like Icelandic Basalt is problematic. Field application is too often unsuccessful because of the knowledge gap in our understanding of the interplay of mechanisms that govern success or failure of the water jetting to penetrate different rock types in downhole reservoir jetting conditions. In the absence of theoretical understanding, water jetting trials are performed on rock samples in ambient atmospheric conditions, hoping to predict from this the jet-ability down hole but to date, laboratory rigs do not have the capability to reproduce the complex reservoir formation pressures, nozzle pressures and true-triaxial stress fields that rock experiences under jetting. Furthermore, modern nozzle designs are evolving with some designs aiming to create pulsating jets and cavitation jets to ROP. The anecdotally reported experiences of different operators (little is recorded in open literature) remain contradictory when describing factors favouring jet-ability, such as ‘greater depths make jetting easier’, ‘increased confinement inhibits penetration’. Guidance on jet-ability remains subjective and poor with only very general published advice available such as; ‘difficulties in penetration are encountered with rocks with porosity of less than 3 or 4%’ (Kamel, 2017).

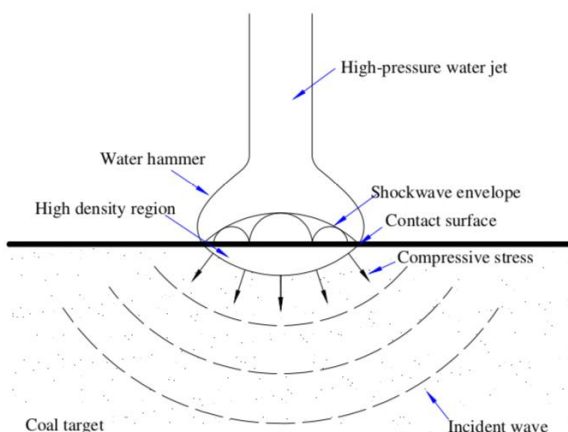


Figure 1. Mechanics model of high pressure water jet impinging on a coal target (Zhao and Guo 2018)

A review of RJD literature (SURE D3.1 report, Blöcher et al., 2016) found very limited reference to mechanisms of jet-rock breakdown. Hypotheses of breakage mechanisms are derived mainly from laboratory studies together with numerical methods which for such complex interacting processes present similarly tentative ideas. Coupled jet-rock numerical models are in their infancy and are under active development.



The SURE project has received funding from the European Union’s Horizon 2020 research and innovation programme under grant agreement No 654662.

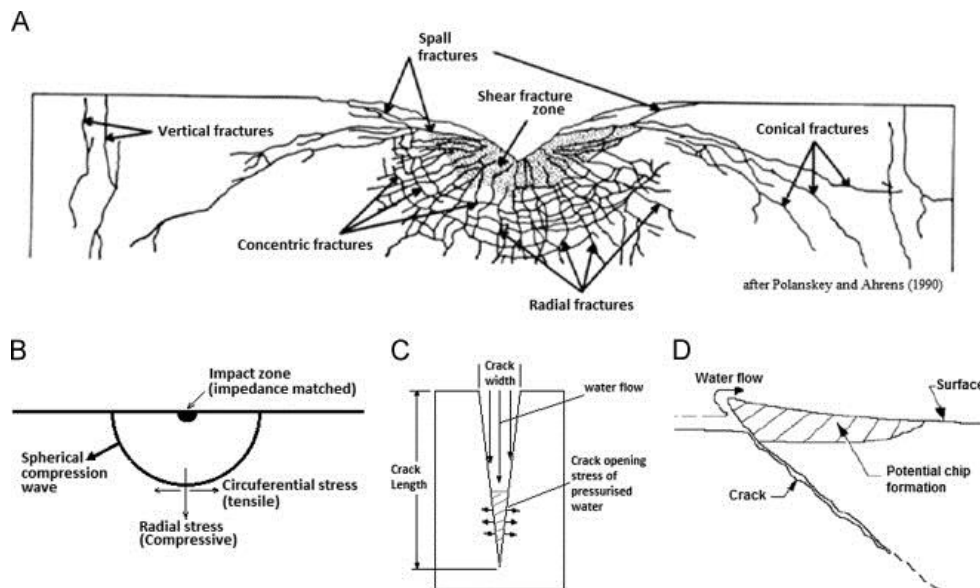


Figure 2. Collisional damage fracture patterns of Polansky and Ahrens (1990) and mechanisms proposed for crack development in water jet drilling as summarised by Dehkoda and Hood (2013), see text.

The breakage and erosion potential of the water hammering effect of a water jet impact were studied by Lu et al., (2015) for sandstones and by Zhao and Guo (2018) for coal. Dehkoda and Hood (2013) examined pulsed jet damage to granite and marble and based their interpretations of crack development on impact cratering phenomena e.g. (Polansky and Ahrens, 1990) see Fig. 2 (A,B) and on fluid driven crack extension (C) as well as shear flow plucking of asperities (D). They also observed confinement of the rock inhibited tensile fractures from running directly in the jet direction for their non-porous rock types. Radial cracking and circumferential tensile spalling cracking is consistent with Zhao and Guo's conclusion that the damage to the far-field coal particles due to the water jet is primarily caused by tensile stress, and the damage to the near-field coal particles by water jet is caused by the coupled effects of tensile stress and compressive stress.

Successful penetration with RJD was observed in a high porosity (Gildehaus) sandstone quarry test (Reinsch et al., 2018) and therefore for low in-situ stress confinement and in-situ pore pressures compared with reservoir conditions. To better understand in-situ stress effects on drilling rate, jetting under true triaxial stress conditions was conducted using the same sandstone, (see D5.2 Hahn et al., 2019). For this set-up and rig, no control over the near to atmospheric pore water pressure inside the 300 mm cube sandstone specimen was possible, however, the study showed that penetration rate varied greatly with stress ratio and drill direction. Faster ROP occurred with maximum stress at right angles to the jetting direction. From detailed imaging of the microstructure of jet-hole surfaces, the modes of grain separation and grain splitting are very local to the hole surface. It can be concluded that for jetting mechanisms to be successful at removing grains and mineral fragments, it will be a consequence of microstructural strength associations between mineral grains and within grains that are active just under and near to the jet. That is to say, the zone of influence and the zone of fracture damage of the jet-to-wall rock pressure and stress fluctuations caused by the jet action



The SURE project has received funding from the European Union's Horizon 2020 research and innovation programme under grant agreement No 654662.

perturbing the background stress field is small and occupies scales of the order of say, ten grains around the jet hammer impinging zone.

The pulsed water jet investigations by Dehkoda and Hood (2013) have motivated further explorations in D5.4 by Gradzki et al., (2019) into the potential for more effective use of water jetting into harder rocks under in-situ pressure conditions by the use of pulsation-assisted water jetting. The investigations aimed to apply pulsating water jets under elevated pressure conditions. The rock specimens were held under a hydrostatic pressure confinement such that the rock mean stress is held at the same level as the saturated pore water and values from 0 to 40 MPa were jetted into with just one or two or five or ten pulses. The results were not conclusive other than the fact that higher confinement back pressures help inhibit the jetting action. Whether this is due to the simultaneous suppression of cavitation remains uncertain. The results were inconclusive about whether several pulses were more effective than just one and this may be due to the pulsation frequency and duration of the jetting requiring further experimental control and for more tests for statistically representative results for a given rock type. The report suggested much more detailed research into pulsed jetting and with shortest pulses would be highly desirable.

Ideally, to capture the most realistic mechanisms and processes of jet drilling for the wide spectrum of rock types into which geothermal resources may be extracted in future, will require a modelling approach that can capture such microstructural strength effects. However, a more pragmatic first-step approach, to simplify the already complex coupled problem, is to consider what we might call a ‘mesoscale’ representation of the rock as homogeneous and isotropic. Such an approach may be less justified for sandstones than, for example, mono-mineralic low porosity rocks such as marble and quartzite.

Although cavitation action of bursting fine bubbles is known to accelerate cutting efficiency of water jet cutters, the theory presented by Li et al, (2014) has cast doubt that bubble bursting is the process whereby cavitation jet drilling is effective in giving improved penetration rate. Indeed, they also suggest that downhole in a well, reducing the pressure in the nozzle from the static pressure to the vapor pressure needed for bubbles is possible extremely difficult.

In order to understand the mechanisms of the rock breakdown and erosion by RJD, several studies have already turned to numerical methods to investigate the interaction between a high velocity fluid and solids. Sakaguchi et al., (2013) developed a three-dimensional Smoothed Particle Hydrodynamics (SPH) method code for the numerical simulation of the interaction between soft rock and a high speed water jet. SPH is a Lagrangian reference frame method that tracks the water flow as a representation of water particle motions which makes coupling with the material solids (also Lagrangian) easier. They proposed five types of failure criteria in the simulation of water jet drilling: 1. Tensile strain criterion; 2. Traveling distance criterion; 3. Equivalent strain criterion; 4. Stress criterion; 5. Mohr-Coulomb criterion. They found that the tensile strain criterion, i.e. failure of their solid occurs when an elastic bond exceeds a certain extensional strain, gave simulation results consistent with the experimental results. Liu et al., (2015) also used an SPH model of the water jet coupled to a finite element method (FEM) representation of the rock response. They investigated the effect of water jet diameter, jet angle and velocity of water jet on the efficiency of rock cracking, in which the mechanism of water jet impacting rock was shown through analysing the impact momentum and stress field and



The SURE project has received funding from the European Union’s Horizon 2020 research and innovation programme under grant agreement No 654662.

energy of rock, mean cutting depth and cutting width. In a similar paper (Jiang et al., 2014), the coupled SPH/FEM method was used to study the rock fragmentation mechanism and propose conditions of impact load of the water jet under which crushing zones form, and conditions for crack initiation and propagation. The maximum principal stress criterion was used for the rock failure criterion. They found that the main mechanism of the rock fragmentation by water jet impact is the combination of shear and tensile failure.

However, these studies have only considered the application of a water jet to rock under simplified assumptions of ambient conditions i.e. no confining stress, a reasonable starting point which may be appropriate for comparison with most rock jet experiments to date. To examine the state of stress locally affecting rock material, i.e. mineral grains near the jet and under the influence of the RJD excavation process occurring in the subsurface, the geomechanical conditions which can vary greatly and are known to influence rock strength and breakage processes, will be important to include for more realistic models of RJD field behaviour. Not only will the direction of drilling in relation to the principal stress directions and the principal stress ratios be important to predict jet-wall stability and presumed excavatability but also, the reservoir formation pore pressure magnitude, via its influence on effective stresses, can profoundly affect fracture initiation and propagation conditions and the pore pressure gradients near the hole are likely to be important. A rock-jetting model that can build in these geomechanical process and have the (poro-elastic) solid rock perturbed by the action of inertia-dominated water jet flows would seem to be a minimum starting point for a predictive model.

Recently, an advanced loose coupling fluid-solid model (the coupling projects fields iteratively between a solid and a fluid mesh rather than solving monolithically over just one mesh for the whole solid fluid system) was developed by Vire et al., (2012, 2015). Yang et al., (2016, 2017) further improved this model with applications including rock blasting by introducing the fluid stress terms into the coupling term. The stress terms enable the model to capture some viscous behaviour in the FSI (Fluid-Structure-Interaction) model simulations.

This report presents a new Immersed Body Method (IBM) coupling development in which a FDEM solver for solids deformation and interactions (Munjiza, 2004; Xiang et al., 2009) (note, the FDEM solver code is continuously being upgraded and managed under Solidityproject.com) is coupled to other modelling technologies e.g. CFD, interface tracking, porous media etc. The CFD solver, Fluidity (Pain et al., 2005; Pain et al., 2001) is a general purpose multiphase CFD code capable of modelling a wide range of fluid phenomena involving single and multiphase flows. The Fluidity project's history has led to several novel advanced methods based upon adapting and moving anisotropic unstructured meshes, and advanced combined finite element and control volume (CVFEM) discretisation. This report aims to create the numerical tools necessary and then to use them to understand more deeply the rock fragmentation mechanism and to explain the reasons for crack initiation, propagation and fragment removal under the impact load of a high-speed water jet. It also aims to investigate the effect of pore water pressure on rock jet drilling performance.

In addition to the above background on modelling technology, we include here the previous research on microstructure representation as background to the new techniques developed here for jetting.



The SURE project has received funding from the European Union's Horizon 2020 research and innovation programme under grant agreement No 654662.

2.2 Reconstruction of rock microscale model

Rock properties including elasticity modulus, tensile strength, toughness, etc. are extensively used for the mesoscale or macroscale analysis of deformation, fracture and other problems. These bulk parameters well describe the property of rock in resisting deformation, fracture and other impacts without complex microstructure becoming involved. However, when it comes to the cases where the microscale failure process mechanisms need to be focused on, the macroscale parameters no longer satisfy the demand. For example, in the context of water jet drilling, the sandstone grains are flushed from the rock mass by the water jet which has a diameter of only 2 mm. Thus, the investigation of microscale rock failure is significant to understand the macroscale response of the rock in specific scenarios, like water jet drilling.

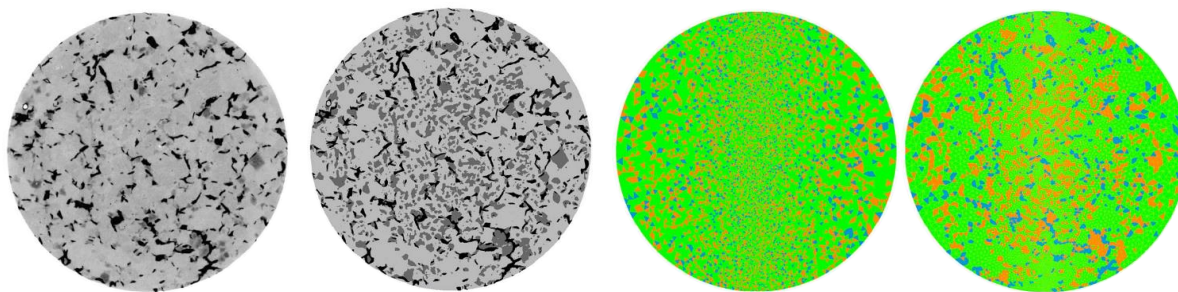


Figure 3. Construction of a granite sample (Mahabadi et al., 2014) from left to right: CT-scan image, segmented image, microstructure based on a discrete Poisson distribution and microstructure based on projection of the CT-scan image.

The rock microstructure has been considered in numerical simulation via different kinds of approaches. The simplest approach is to generate the numerical mesh firstly and to assign the phase type or properties to the mesh elements according to specific stochastic distribution or artificially (Mahabadi et al., 2014), as shown in Figure 3. Alternatively, a Voronoi diagram might be generated firstly and then the Voronoi polygons are assigned with different phase types to present the interaction between rock grains (Gao et al., 2016; Peng et al., 2017; Gao and Kang, 2017; Ghazvinian et al., 2014; Gui et al., 2016; Li et al., 2017a; Li et al., 2017b; Liu et al., 2018). Although the component ratio or porosity could be easily satisfied in both the two approaches, the pattern as seen in a typical rock sample for the distribution of different components is completely missing. Another approach is to project the actual mineral distribution from digital rock images onto the numerical model (Chen et al., 2004, 2006; Lesueur et al., 2017; Li et al., 2019; Mahabadi et al., 2014; Suchorzewski et al., 2018; Yu et al., 2018; Zhao et al., 2014; Zhu et al., 2018). The drawback here is that a smooth boundary between different minerals or grains may become zig-zag after projection and a good presentation of the grain boundaries requires a very fine mesh.

Stochastic reconstruction is a kind of technique to reconstruct a sample which has the same stochastic information with the target sample, as shown in Figure 4. In the traditional stochastic reconstruction method, there are two essential tasks: assigning descriptors and assigning the reconstruction method. The descriptors are the mathematical stochastic parameters to describe some specific characteristics of the target sample, such as volume fraction, connectivity, etc. Reconstruction method is the approach used for generating the reconstructed image. By choosing a suitable descriptor, the specific information from the target image, such as the volume fraction, or distribution of the materials, can be kept in the reconstructed image.



The SURE project has received funding from the European Union's Horizon 2020 research and innovation programme under grant agreement No 654662.

However, these kinds of methods normally only work for the pixel-based square image which at resolutions obtained directly from X-Ray CT imaging has a number of pixels greatly beyond the computation capacity of the numerical model. Extra developments are needed to construct the microstructure for use in a numerical model which consists of the mesh or particles. Therefore, the development of a work flow to incorporate the actual complex rock microstructure into the numerical model with a reasonable accuracy and practical computation cost, even in 2D, remains a challenge.

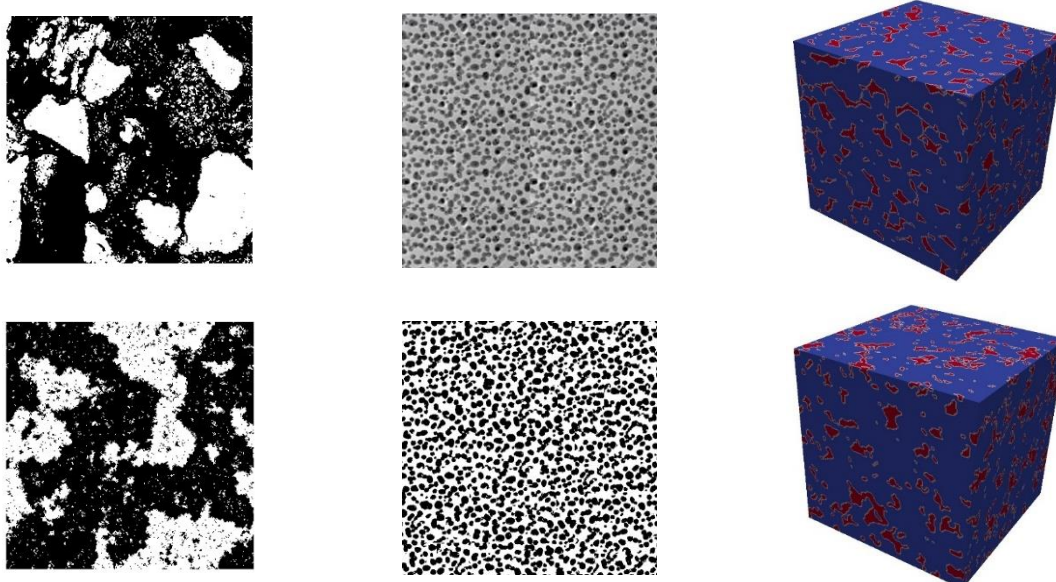


Figure 4. Stochastic reconstruction technique: target image (top) and reconstructed image (bottom)

3 Mesoscale simulation of water jet drilling

3.1 Immersed Body Method (IBM) for water jet drilling

The new immersed body method is used for simulating rock fragmentation mechanism of water jet drilling. Coupling between solids and fluids is realised using a three-mesh approach. One mesh (fluid mesh) is used across the whole solution domain on which the fluids equations are solved and the second mesh (solid mesh) contains a finite element representation of the solid (possibly fracturing and fragmenting) structures. The third mesh (thin shell mesh) acts as a numerical delta function in order to help apply the solid-fluid boundary conditions. Adaptive meshing (Piggott, et al. 2001, Yang, et al. 2006) resolves down onto the complex geometry of the solids at the level of detail necessary, hence addressing one of the main challenges – the accuracy of the flow field near the solid surfaces and the capture of boundary layer effects. The forces and volume fraction of solid from the FDEM structure model are mapped onto the fluids mesh using FEM mapping and updated hydraulic forces are returned to the explicit transient dynamic FDEM modelling of the solids. The IBM also couples implicit and explicit solvers, i.e. implicit CFD solver for water jet and explicit FDEM solver for solid mechanics. The details of IBM can be found in Yang et al., (2016, 2017).



The SURE project has received funding from the European Union's Horizon 2020 research and innovation programme under grant agreement No 654662.

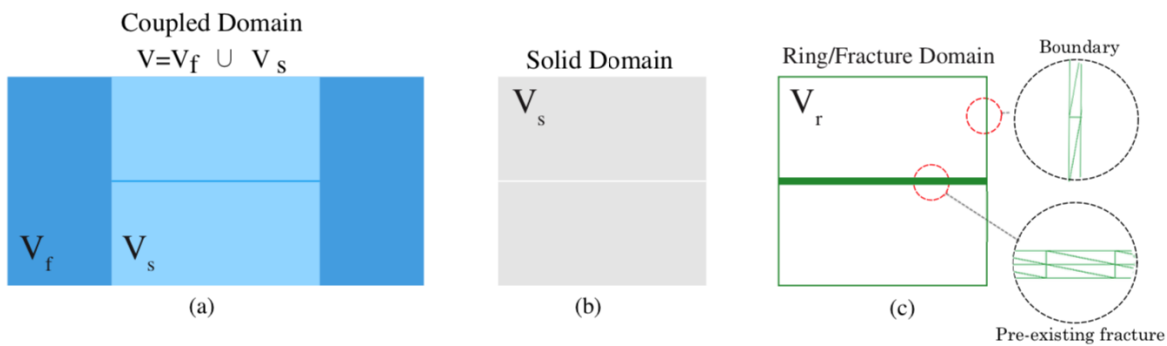


Figure 5. Schematic of the immersed-body method: (a) the solid domain V_s is fully immersed in the fluid domain V_f in the flow simulation; (b) the solid domain V_s is used in the geomechanics simulation; and (c) the ring mesh V_r is generated surrounding the solid domain with the ring thickness defined by the aperture along fractures or by a near-zero value at the boundary (Obeysekara, 2018)

3.1.1 Equations for solid dynamics

For the structural dynamics, FDEM is used in our model. The finite discrete element method initially developed by Munjiza et al. (1995) is specially designed for simulating rock mechanics problems and has great advantages in simulating rock deformation and failure (Tatone and Grasselli, 2015; Lisjak et al., 2018; Ma et al., 2017). It is capable of simulating the transition process of the intact rock to discrete parts. In the FDEM model, the intact rock is discretised into triangular elements in 2D or tetrahedra elements in 3D. The elements next to each other are connected with the so-called joint elements which have non-linear responses to the relative displacement between the elements. Once the relative displacement between the elements are beyond certain criteria, the joint element between them are assumed to be broken in specific type (tensile and shear) according to the criteria satisfied. The interaction between the elements belonging to different fracture surfaces in a single body or external surfaces from multi-bodies are computed according to their overlap in space.

The dynamics of the solid model is given by equation 1:

$$\mathbf{F}_{ext} - \mathbf{F}_{int} + \mathbf{F}_c + \mathbf{F}_p + \mathbf{F}_d = \mathbf{M}_s \frac{\partial \mathbf{u}_s}{\partial t} \quad (1)$$

where, \mathbf{F}_{ext} and \mathbf{F}_{int} denote the external and internal force, respectively, \mathbf{F}_c is the contact force when collisions happen among multiple solids, \mathbf{M}_s represents the mass, \mathbf{u}_s is the solid velocity, t denotes the time, \mathbf{F}_d and \mathbf{F}_p are the exchange forces between the fluid flow and solids due to the fluid pressure and viscous terms.

3.1.2 Equations for fluid dynamics

‘Fluidity-Multiphase’ (Pain, et al. 2005, Pain et al. 2001), an open-source finite-element CFD model, is used here to model fluid flow. The continuity equation is:

$$\nabla \cdot \mathbf{u}_f = 0 \quad (2)$$



The SURE project has received funding from the European Union’s Horizon 2020 research and innovation programme under grant agreement No 654662.

where u_f is the fluid velocity.

The momentum equation is given as follow:

$$\rho_f \frac{Du_f}{Dt} = -\nabla(p - \tau) + \mathbf{B}_f + s_t \quad (3)$$

where ρ_f is the fluid density, p denotes the fluid pressure, τ is the deviatoric stress tensor due to viscous effects, \mathbf{B}_f represents the body force per unit mass (e.g. gravity), s_t is the coupling term, which gives out the effect of the solid motion on turbulent flow.

In order to embed the solid equations into the fluid equations, a supplementary equation connecting the solid and fluid velocities is given as follow:

$$\hat{\sigma}(u_s^s - u_f^s) = \hat{\sigma}(\hat{u}^f - u_f^f) \quad (4)$$

where u_s^s and u_f^s represent the solid velocity on solid mesh and fluid velocity on solid mesh, respectively, u_f^f is the fluid velocity on fluid mesh, $\hat{\sigma} = \frac{\rho_f}{\Delta t}$, and $\hat{u}^f = \alpha_f u_f^f + \alpha_s u_s^f$, where α_s represent the fluid and solid volume fraction, respectively, Δt is the fluid time step. In this paper, the superscripts f and s refer the value on the fluid and solid mesh, respectively, and the subscripts f and s represent the value of the fluid and solid, respectively. Thus, the continuity equation can be rewritten as:

$$\nabla \cdot \hat{u}^f = 0 ,$$

where:

$$\hat{u}^f = \begin{cases} u_s^f & \text{when } \alpha_f = 0, \alpha_s = 1 \\ u_f^f & \text{when } \alpha_f = 1, \alpha_s = 0 \end{cases} \quad (5)$$

3.1.3 Fracture model

The three-dimensional fracture model used in this paper was developed in the context of FDEM in the Dr Guo's PhD project (Guo, 2014). In his thesis, the cohesive zone fracture model (CZM) has been implemented. In the FDEM simulations, the entire domain is treated as a multi-body system and each discrete element is further discretised into a mesh of finite elements. The finite element formulation is used to simulate continuum behaviour for each discrete body, which includes the calculation of strain and stress in finite elements. The discrete element formulation is used to simulate discontinuum behaviour, e.g. contact interaction between discrete bodies and across discontinuities, which means the calculation of contact force and the distribution of contact force to finite element nodes. The fracture model links the finite element formulation with the discrete element formulation. For each intact discrete body, before fracture initiation, the stresses are calculated by the finite element formulation; if the stress state meets the failure criterion, a discrete fracture will form and then the interaction between discrete fracture surfaces will be modelled explicitly by the contact algorithms in the discrete element formulation; therefore, the whole process of transition from continuum to discontinuum can be realistically and accurately captured.



The SURE project has received funding from the European Union's Horizon 2020 research and innovation programme under grant agreement No 654662.

3.1.4 Pore pressure

The original formulation of Biot theory (Detournay and Chen, 1988) is used in this study. The total stress σ and the pore pressure p can be expressed as follows:

Total stress:

$$\sigma_{ij} = 2G\varepsilon_{ij} + \lambda\delta_{ij} - \alpha\delta_{ij}p \quad (6)$$

Pore pressure

$$p = -\frac{2GB(1+\nu_u)}{3(1-2\nu_u)} + \frac{2GB^2(1-2\nu)(1+\nu_u)^2}{9(\nu_u-\nu)(1-2\nu_u)}\zeta \quad (7)$$

Effective stress

$$\sigma'_{ij} = \sigma_{ij} + \alpha\delta_{ij}p \quad (8)$$

where δ_{ij} is the Kronecker delta, G is the shear modulus, ν is the Poisson's ratio, ν_u is the undrained Poisson's ratio, assuming $\nu_u = \nu/0.6$, B is Skempton's pore pressure coefficient, α the Biot's coefficient.

In this study, it is assumed that the RJD rock breakdown process is under undrained conditions as pore water is unable to drain out of the rock in response to the impact of the water jet. This is reasonable as this paper focuses on what is breaking the rock under the very short time-scales of the transient behaviour of jet-rock impact interaction. Consequently, the second term of the pore pressure equation can be ignored, and the pore pressure and the correction to the stress field, via α can be derived as follows

$$p = -\frac{2GB(1+\nu_u)}{3(1-2\nu_u)}\varepsilon \quad (9)$$

$$\alpha = \frac{3(\nu_u-\nu)}{B(1-2\nu)(1+\nu_u)} \quad (10)$$

3.2 Numerical simulation setup and material properties

The model setup is shown in Figure 6. The rock specimens are in the form of a slice with a diameter of about 50 mm and a thickness of 20 mm. Figure 6 shows a sketch of a rock specimen with dimension and target zones for the high-pressure water jet to act on. The standoff distance between rock surface and nozzle outlet is 6 mm and the diameter of orifice is 2 mm. The exiting nozzle velocity magnitude varies from 0 m/s (nozzle wall) to 320 m/s (middle of nozzle), resulting in average velocity of 160 m/s (see Figure 7).

Three rock types, Gildehaus sandstone, Dortmund sandstone, and Icelandic Basalt, are used in this study. The material properties of the rocks are measured in The Helmholtz Centre Potsdam - GFZ German Research Centre for Geosciences and listed in Table 1.



The SURE project has received funding from the European Union's Horizon 2020 research and innovation programme under grant agreement No 654662.

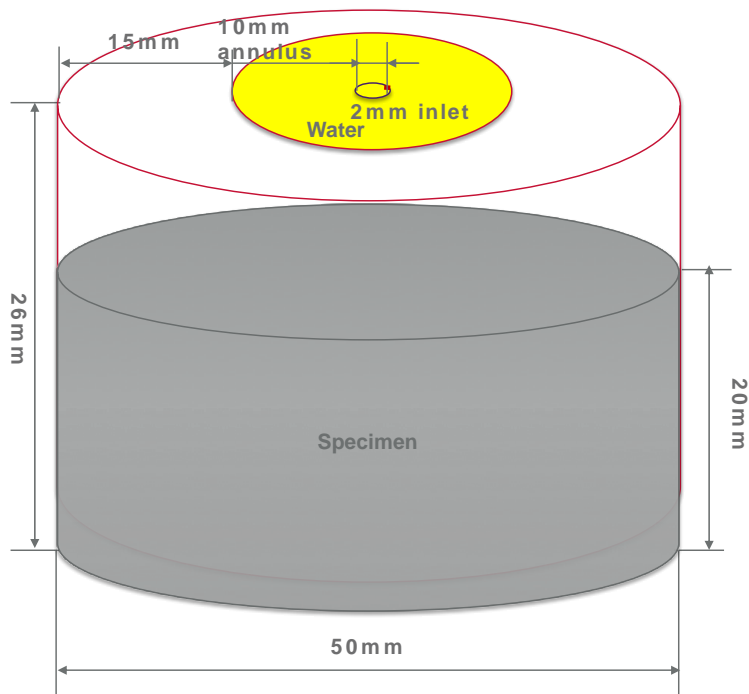


Figure 6. Sketch of simulation setup

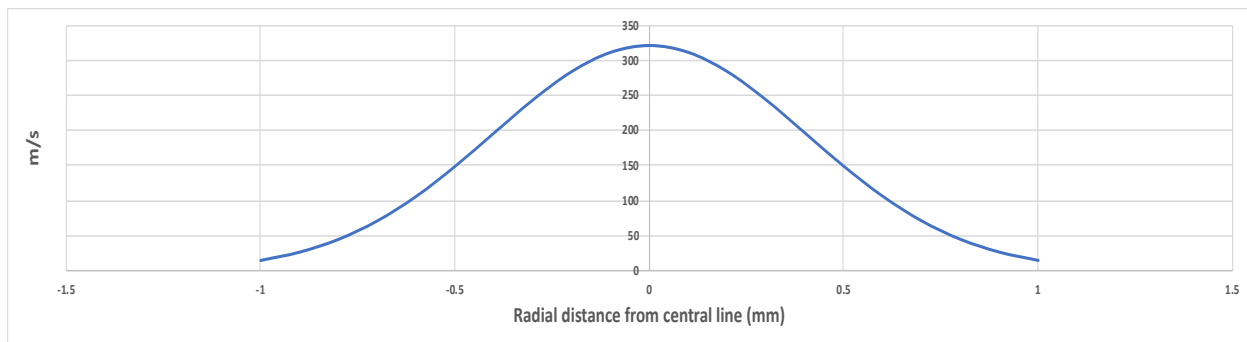


Figure 7. Exiting water velocity distribution

Table 1. material properties

	Gildehaus	Dortmund	Icelandic Basalt
Young's modulus E GPa	19.5	21	17
Poisson's ratio v	0.265	0.12	0.22
Bulk Density (kg/m ³)	2000	2425	2750
Tensile strength MPa	3.5	7.2	7.16
Internal friction angle	23	25	35
Cohesion MPa	17.5	22	38.5
UCS MPa	53	69	148
Gic J/m ²	8.2	30.5	43.5
Giic J/m ²	171.7	637.9	910.6

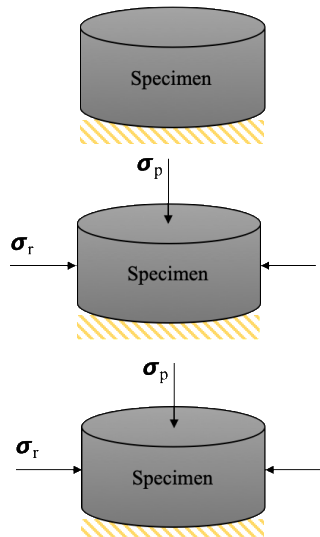


The SURE project has received funding from the European Union's Horizon 2020 research and innovation programme under grant agreement No 654662.

3.3 Boundary conditions

Table 2 shows the boundary conditions of the simulations, i.e. the bottom of specimen is fixed, and appropriate constraint conditions (such as pressures or stress confinement) can be applied to the remaining surfaces.

Table 2. Boundary conditions

Not considering pore water pressure	Considering pore water pressure
 Specimen σ_p Specimen σ_r Specimen σ_p σ_r	
Case 1-3, in Atmospheric condition, bottom fixed	
Case 4 $\sigma_p=0.1\text{ MPa}$ $\sigma_r=5\text{ MPa}$ bottom fixed	Case 6 $\sigma_p=0.1\text{ MPa}$ $\sigma_r=5\text{ MPa}$ bottom fixed
Case 5 $\sigma_p=2.5\text{ MPa}$ $\sigma_r=5\text{ MPa}$ bottom fixed	Case 7 $\sigma_p=2.5\text{ MPa}$ $\sigma_r=5\text{ MPa}$ bottom fixed

3.4 Results and discussions

3.4.1 Mesh adaptivity

The fluids simulation is computed based on an adaptive mesh which refines the mesh according to the proximity of the interface of the rock and the fluid velocity gradient, as shown in Figure 8. The minimum mesh edge size is 0.2 mm and the maximum mesh edge size is 5 mm. The fluid mesh used by the fluid code in the coupling model is very refined near the fluid jet and vortices, and relatively coarse elsewhere.



The SURE project has received funding from the European Union's Horizon 2020 research and innovation programme under grant agreement No 654662.

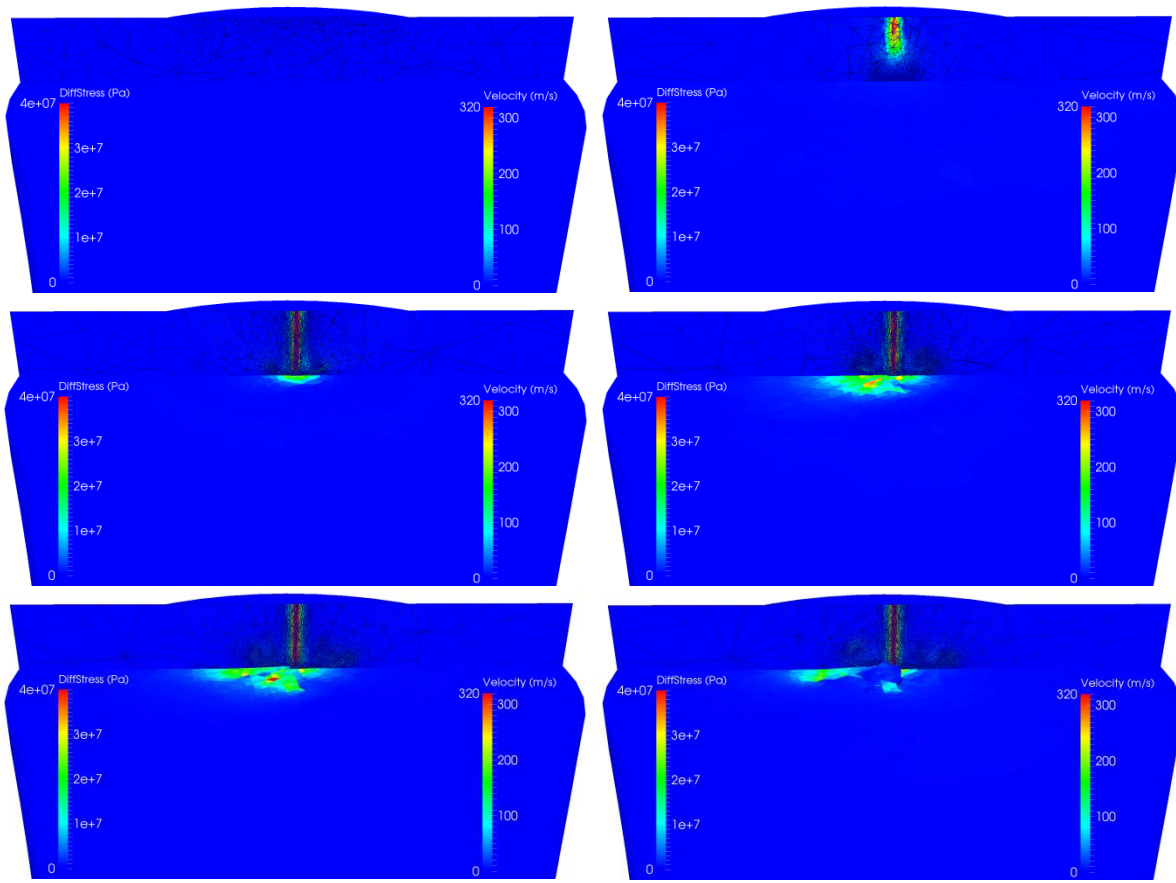
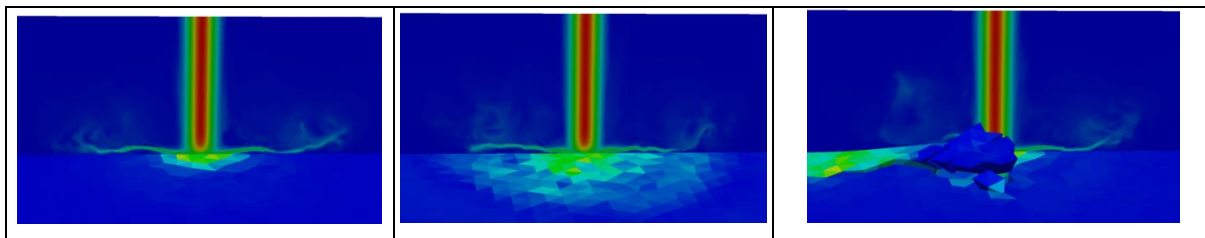


Figure 8. Six stages during the jetting action focusing on the impulse phase. Adaptive mesh refinement responding to water jet velocity together with stress development in the solid target. Cut plane shows fluids mesh and flow velocity colours shown on right side legend. Differential stress in solid rock cylinder, left hand legend. (Gildehaus Sandstone Case 3).

3.4.2 Effect of rock strength

There are three rock types simulated in this paper using their laboratory determined average properties: Gildehaus Sandstone, Dortmund sandstone, and Icelandic Basalt. Gildehaus Sandstone has the smallest tensile strength 3.5 MPa, and the lowest mode I & II energy release rates, 8.2 J/m² and 171.7 J/m² respectively, (see Table 1). As shown in Figure 9, only Gildehaus Sandstone can be eroded and cracked under water jet impact. The other two rocks have no fragment removal, although Dortmund Sandstone showed the stress state was near to inducing minor damage. This qualitatively agrees with experimental observations.



The SURE project has received funding from the European Union's Horizon 2020 research and innovation programme under grant agreement No 654662.

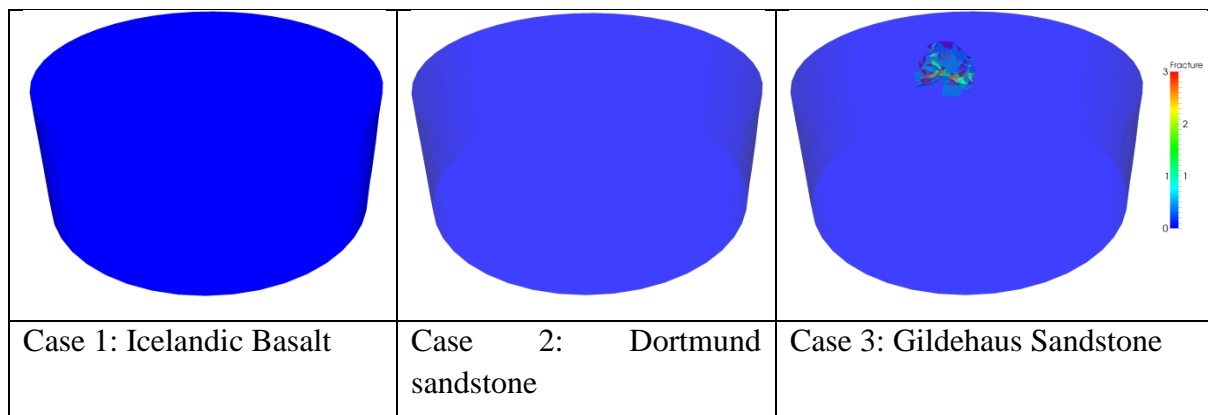


Figure 9. Crack initiation and propagation corresponding to high speed jet drilling for different rock types and strength and physical properties assuming pore pressure in the rock remains constant. (Table 1): a) Icelandic Basalt b) Dortmund sandstone; c) Gildehaus Sandstone.

3.4.3 Failure mechanism analysis

The most important objective of this modelling research is to understand the mechanism of jetting erosion. It is very difficult to judge the main failure mode from experimental measurement. However, we can extract components of the stress tensor from numerical results and analyse the principle stress to better understand the failure mode of the cracks generated. For example, Figure 10 left shows the differential stress for solids and velocity field for fluids. Figure 10 right shows the principle stress (σ_1 and σ_3) and differential stress of the element where the first crack generated. It shows at frame 10, from σ_3 (geomechanical stress sign convention means a negative σ_3 is a tensile stress) that tensile stresses exceed 5 which is larger than the tensile strength (3.5 MPa), but the differential stress is above 25 MPa which is larger than Cohesion (17.5 MPa) and may also be sufficient to initiate shear or mixed-mode shear and tensile failure. This is because the high speed water jet impacts on the surface of the specimen and generates a very high water pressure to create radiating compressive waves that have associated tensile hoop stresses. Stress theory for projectile impact and for indentation, can provide insights as to whether the water pressure may be sufficient to break the specimen with radial tension cracks. This phenomenon leading to breakage can be referred to as a “water hammer mechanism”. It is clearly associated with the generation of tensile stress and breakage in tension and may involve some mixed-mode tensile and shear fracturing. However the mechanism is not associated with compressive pulverisation or shear fracture networks. However, the exact failure mode is not known in detail for this combination of water pressure and rock properties. Fortunately, the solid mechanics FDEM code can directly export the failure mode for every crack (see Figure 11). It shows the first crack is tensile failure. Further fracture type analysis shows most of cracks are tensile failure, only 20% of cracks are mixed mode failure and none are pure shear mode.



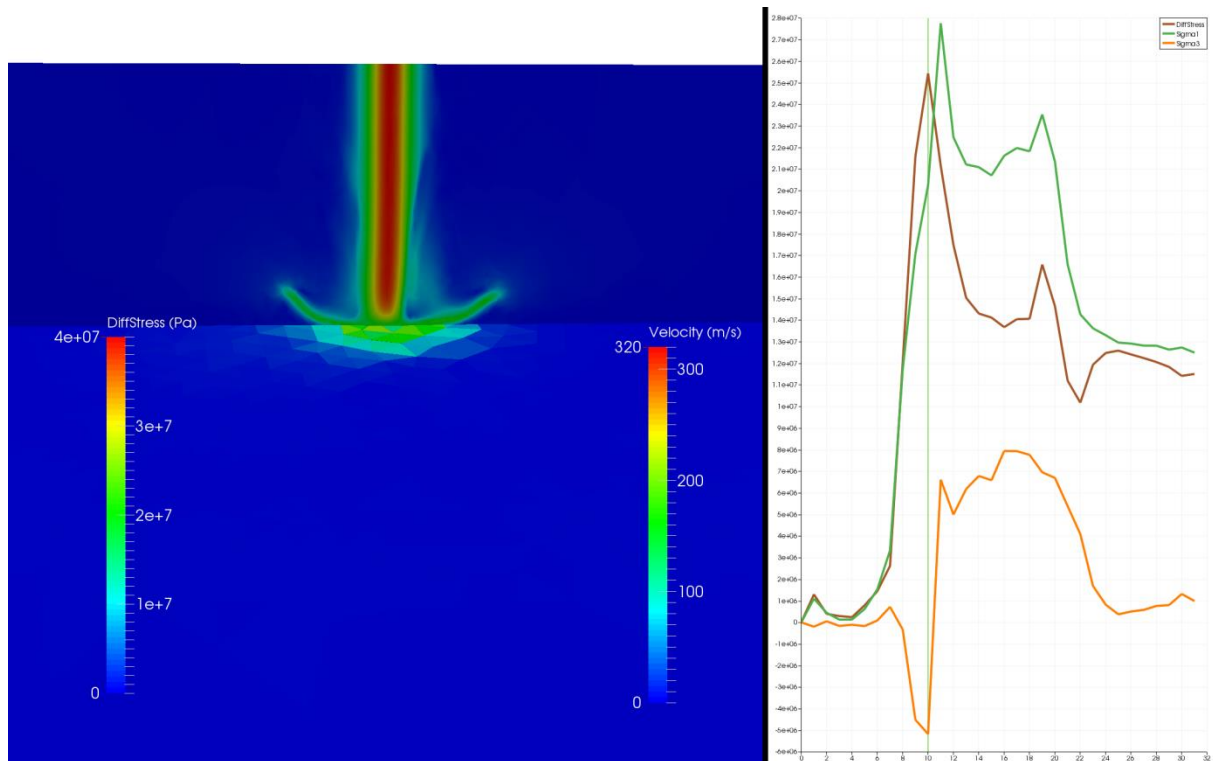


Figure 10. The stress analysis of the first crack

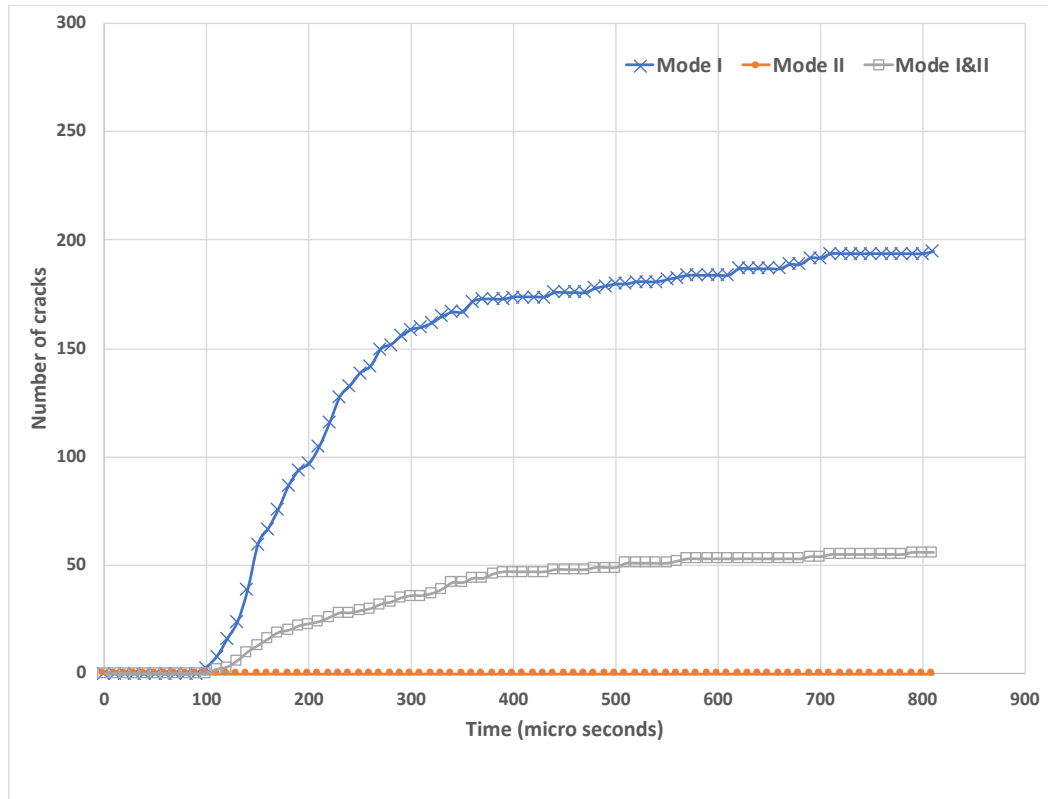


Figure 11. Numbers of cracks in different failure mode vs time



The SURE project has received funding from the European Union's Horizon 2020 research and innovation programme under grant agreement No 654662.

3.4.4 Effect of pore pressure and “water back pressure”

In this study, poro-elasticity is considered and Biot’s theory has been implemented to simulate the effect of the water pore pressure over time and space as the jet’s surge in locally applied water pressure arrives at the specimen surface. To understand the effect of the pore pressure, we re-ran the test shown in Figure 12 but considering the new pore pressure formulation which would hopefully capture the dominant behaviour due to non-constant, (in fact rapid transient changes) in the pore pressure inside the rock as the jet pressure pulse kicks in. The new simulation results are shown in Figure 15 and compared with the previous results shown in Figure 13. It is found that after considering pore pressure transient changes due to the jet pulse arriving, RJD generates cracks in slightly wider areas. For this preliminary scenario considered, with a modest radial confining stress of 5 MPa, the result demonstrates that the transient elevated pore pressure will act to enhance the RJD “jet-ability” but not significantly. The pore pressure only slightly enhances the shear failures in Case 4 in which the sample is under a radial confining stress of 5 MPa and back pressure of 0.1 MPa based on considering the effect of the pore pressure transients arriving.

A water pressure head around the RJD nozzle called “back pressure”, as distinct from the very high pressures impinging on the rock due to the jet, is needed to pump water from the water chamber around the RJD nozzle back to the surface. The effect of the back pressure has not been investigated in the past. In this report, we consider the back pressure by adding it onto the fluid hydrostatic pressure. Some preliminary results are shown in Figure 16. When the back pressure is increased from 0.1 MPa to 2.5 MPa under the same constraint conditions (5 MPa radially on side wall surfaces), the cracking and jet penetration of rock is significantly reduced.

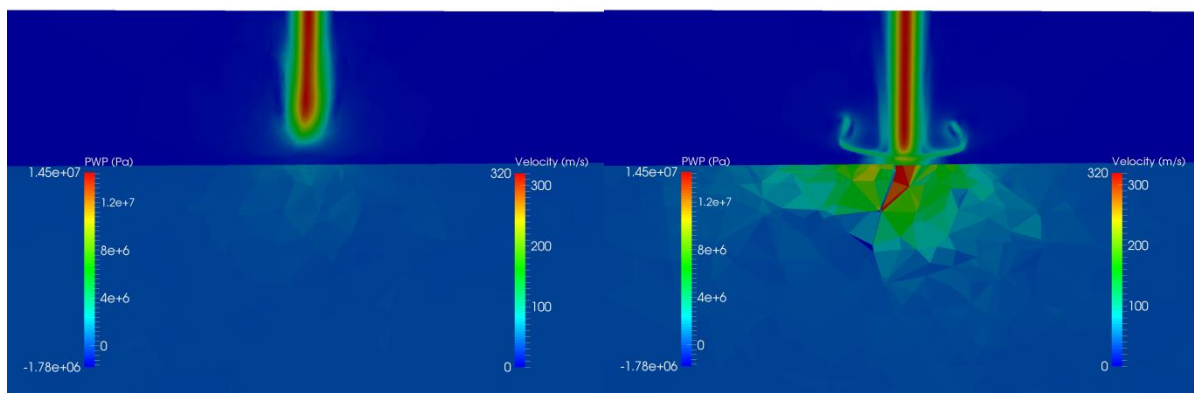


Figure 12. Crack initiation and propagation corresponding to high speed jet drilling in an unconfined rock cylinder considering the effect of the pore pressure transients arriving

System adopted for defining fracture type:

index	Failure mode
3	mixed mode
2	shear failure
1	tensile failure
-1	no cracks or boundary

1. Case 4



The SURE project has received funding from the European Union’s Horizon 2020 research and innovation programme under grant agreement No 654662.

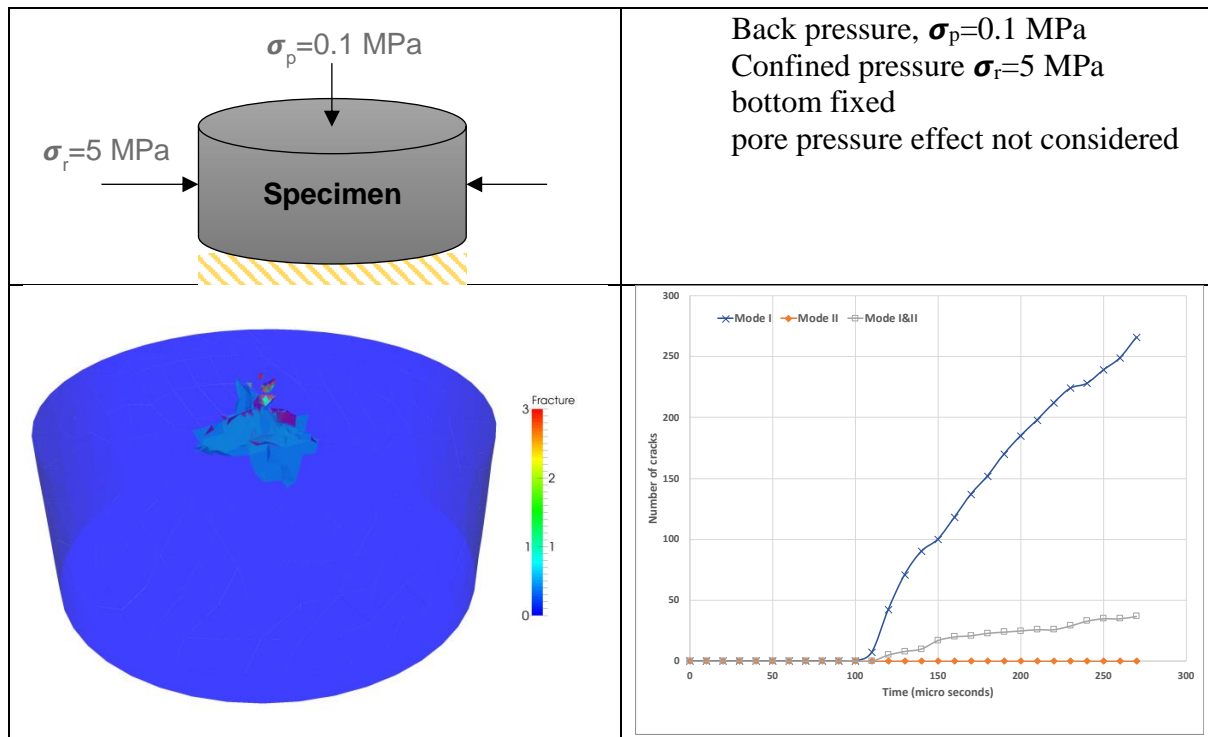


Figure 13. Crack initiation and propagation responding to high speed jet drilling in a radial confining stress of 5 MPa under back pressure of 0.1 MPa, based on no considering the effect of the pore pressure transients arriving.

2. Case 5

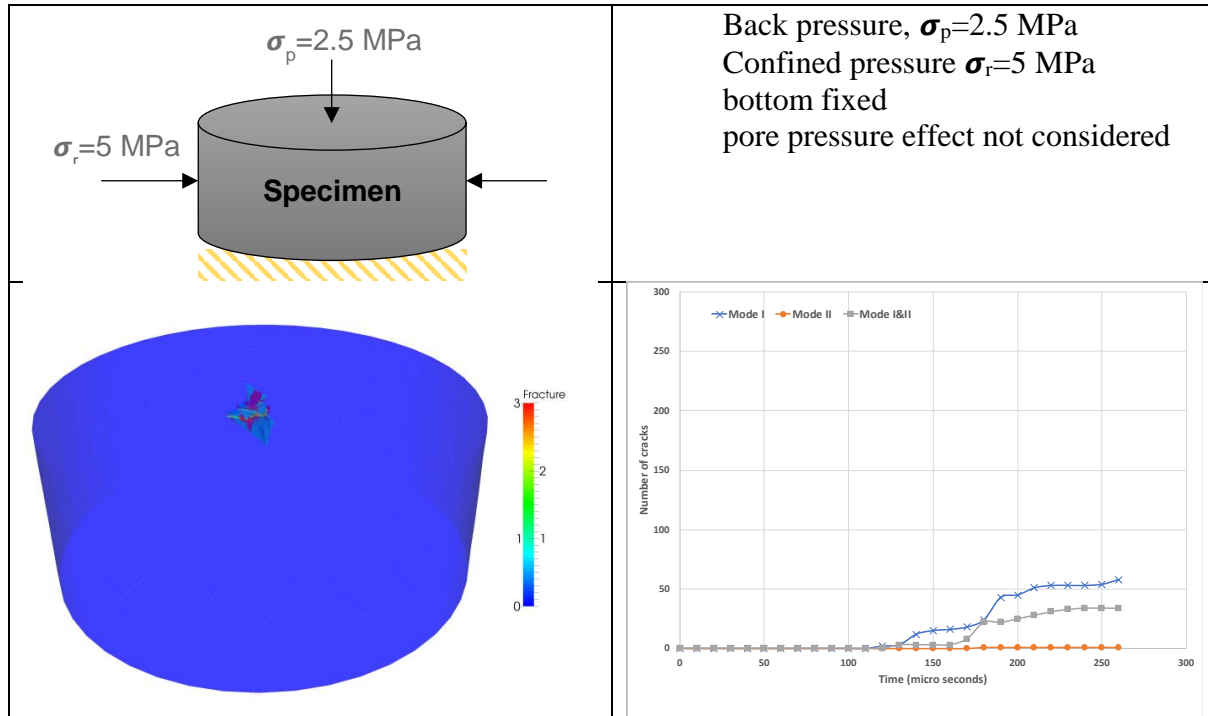


Figure 14. Crack initiation and propagation responding to high speed jet drilling in a radial confining stress of 5 MPa under back pressure of 2.5 MPa, based on no consideration of the effect of the pore pressure transients arriving.



The SURE project has received funding from the European Union's Horizon 2020 research and innovation programme under grant agreement No 654662.

3. Case 6

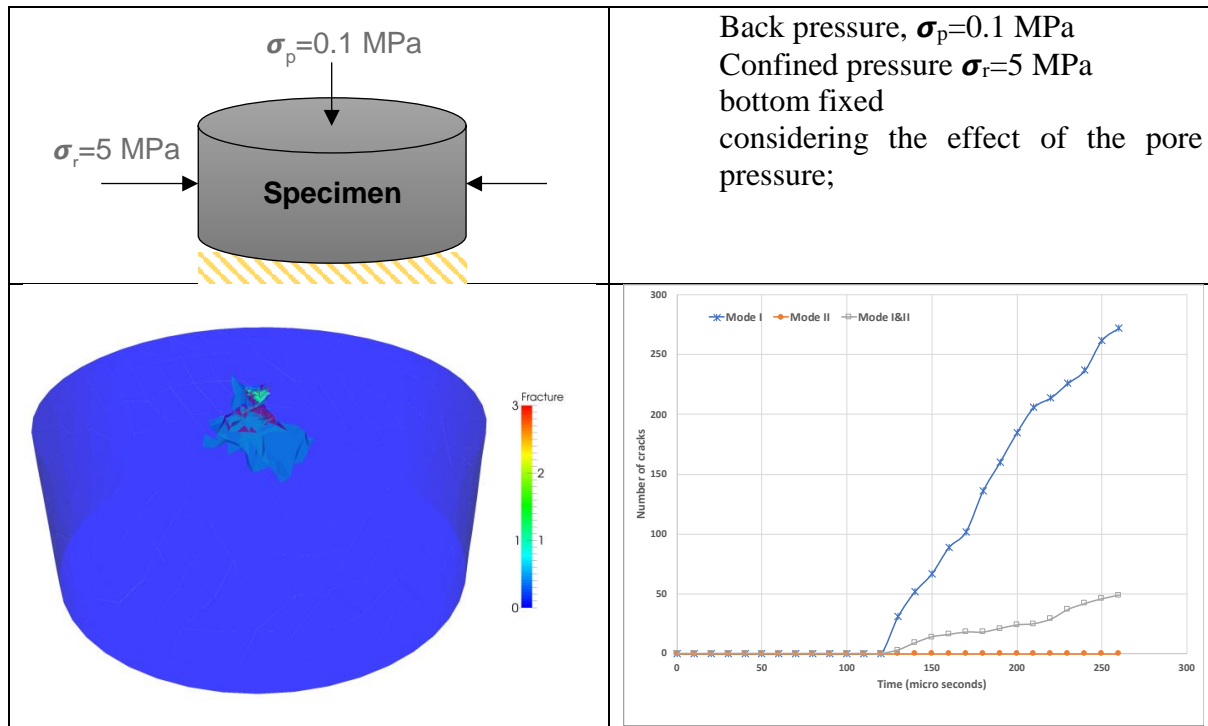


Figure 15. Crack initiation and propagation responding to high speed jet drilling in a radial confining stress of 5 MPa under back pressure of 0.1 MPa, based on considering the effect of the pore pressure transients arriving.

4. Case 7

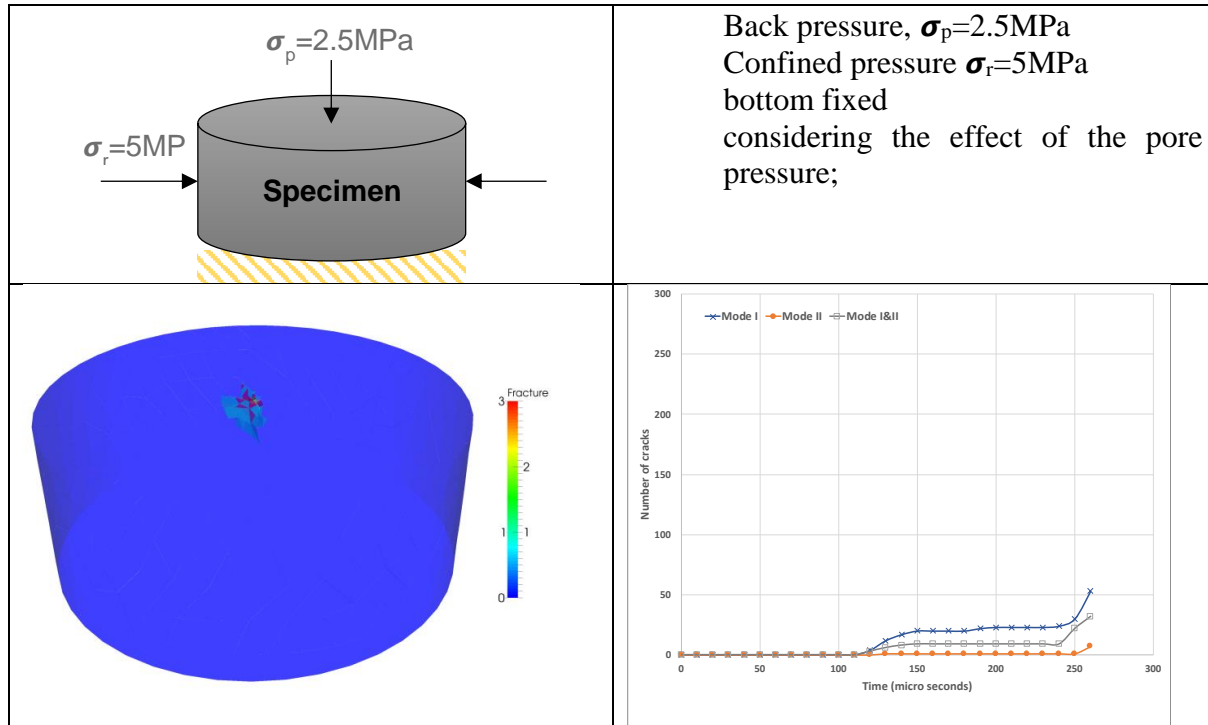


Figure 16. Crack initiation and propagation responding to high speed jet drilling in a radial confining stress of 5 MPa under back pressure of 2.5 MPa, based on considering the effect of the pore pressure transients arriving.



The SURE project has received funding from the European Union's Horizon 2020 research and innovation programme under grant agreement No 654662.

3.5 Conclusions

This report presents a new 3D immersed body method in which the fracture model was incorporated into a two-way fluid-solid coupling model. A methodology of using this model to capture hydraulic fluid-driven fracturing behaviour in high speed water jet drilling was proposed. To investigate the transient effects of the pore water pressure within the rock behind the jet impulse, Biot's poro-elasticity theory for undrained conditions was implemented. The effect of material mechanical strengths was also investigated.

The new fluid-solid coupling model with the fracture model is capable of simulating crack initiation, propagation and fragment removal under the impact load of a high-speed water jet. under the condition of average water exiting velocity 160 m/s and standoff distance 6 mm, atmospheric condition, Gildehaus sandstone can be eroded and cracked under water jet impact while Dortmund sandstone, and Icelandic Basalt are harder to be eroded, which qualitatively agrees with experimental observations. For Gildehaus sandstone, the main drilling mechanism is identified as "water hammer effect". The numerical results show most of cracks are tensile failure, only 20% of cracks are mixed mode failure and none are pure shear mode.

In this section, we also investigated the transient effects of the pore water pressure and the back pressure for Gildehaus sandstone. It is found that after considering pore pressure transient changes due to the jet pulse arriving, RJD generates cracks in slightly wider areas. The result demonstrates that the transient elevated pore pressure will act to enhance the RJD "jet-ability" but not significantly. The effect of the pore pressure transients arriving was considered and the pore pressure change only slightly enhances the shear failures in Case 4 for which the sample is under a radial confining stress of 5 MPa and back pressure of 0.1 MPa. When the back pressure is increased from 0.1 MPa to 2.5 MPa under the same constraint conditions (5 MPa radially on side wall surfaces), the cracking and jet penetration of rock is significantly reduced.

The numerical tests presented in this report show good agreement with experimental results qualitatively. It is worth mentioning that more quantitative benchmark tests, e.g. based on true triaxial compression boundary conditions with in-situ pore-pressure, and ideally for different rock types need to be done to validate the range of applicability of this model. In further work (Section 4 below), we consider the effect of micro-structure on the interaction between high speed water jet and rock specimens as it is likely that the mechanisms important for an understanding of jetting action interact at a scale dominated by microstructure.

4 Microscale simulation of water jet drilling

4.1 Re-construction of microscale model for igneous and porous sedimentary rock

4.1.1 *Re-construction of microscale model for granite with stochastic reconstruction method*

Considering the traditional stochastic reconstruction is normally implemented on pixel-based images, a novel stochastic reconstruction method based on a Voronoi diagram is proposed, as shown in Figure 17. Apart from the target image, a Voronoi diagram is also generated as an input before the reconstruction. The polygons in the Voronoi diagram define the boundary of the grains. Then the pixels in the target image are divided into groups according to the Voronoi polygons. The pixels in the same group are set to have the same kind of material when generating the initial image. Different from the traditional simulated annealing method where



The SURE project has received funding from the European Union's Horizon 2020 research and innovation programme under grant agreement No 654662.

the property for two pixels belonging to different type of material is changed, the property for two groups of pixels belonging to different types of material are swapped. Then the two-point correlation function is extracted and compared with that for the target image. If the difference between them is lower than the similarity acceptance criterion, then the output image is accepted, otherwise another pair of pixel groups is swapped. With the proposed approach, a granite sample is reconstructed, see Figure 18.

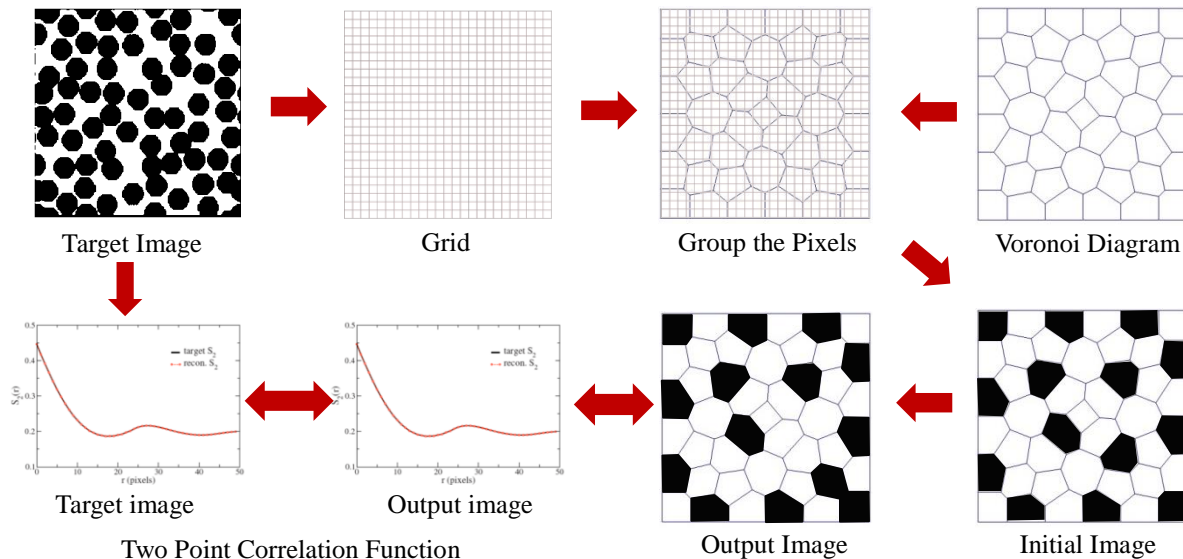


Figure 17. A novel stochastic reconstruction method based on Voronoi diagram

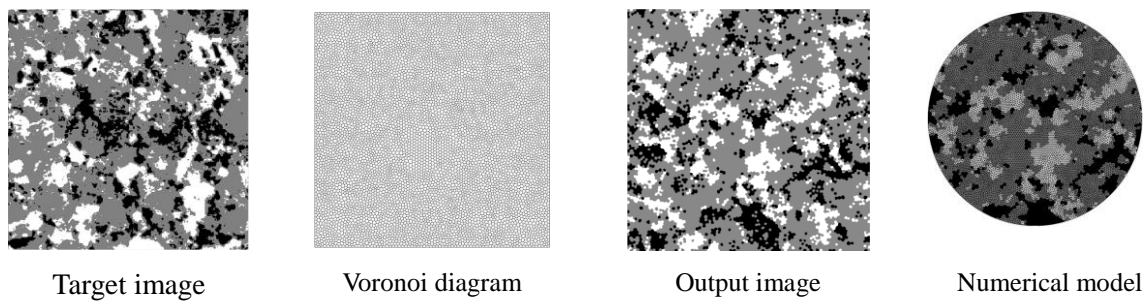


Figure 18. Reconstruction of the granite sample for Brazilian test

4.1.2 Re-construction of microscale model for sandstone with CT-scan data

A novel CT-scan based approach for constructing a sandstone microstructure model is proposed in this section with the objective of constructing the sandstone microstructure in a computational mesh suitable for a specific advanced numerical simulation of rock deformation. Firstly, the sandstone microstructure geometry presented by 3D surface mesh is generated within Avizo software (developed by Thermo Fisher Scientific) based on the CT-scan data. Then the 2D numerical mesh for modelling the sandstone microstructure on a specific plane can be extracted directly from the 3D surface mesh while the 3D tetrahedra mesh is generated based on the 3D surface mesh.



The SURE project has received funding from the European Union's Horizon 2020 research and innovation programme under grant agreement No 654662.

4.1.2.1 Construction of 2D sandstone microstructure model

The construction of the sandstone microstructure model is achieved in Avizo software through a series of treatments including material segmentation, grain separation, surface generation, etc., as shown in Figure 19. The main processes are briefly described here. Firstly, a median filter is applied to the CT-scan data to avoid noises. Then an interactive thresholding is adopted to segment the sandstone grains and pores. Afterwards, the sandstone grains are recognized with a watershed segmentation technique. The grain surfaces are then generated using the Surface Generation tool and are presented by the triangle mesh generated directly from the voxels. The initial mesh for grain surfaces is further simplified to save computation cost.



Figure 19. Construction of sandstone microstructure model in Avizo software: original CT-scan data (left), material segmentation (middle) and particle separation (right).

The 2D numerical mesh for the sandstone microstructure model on a specific plane is extracted from the generated 3D surface mesh. The process is executed via a specifically written MATLAB code and is summarized here. A mesh file for the 3D surface mesh (.hmascii file) is exported from Avizo firstly. A MATLAB code is developed to extract the element information and corresponding grain ID information. Finally, the information for the 2D numerical model are written into mesh files readable for GID, a pre- and post- processor software tool developed by the International Centre for Numerical Methods in Engineering (CIMNE) (CIMNE, 2019). An example of the 2D numerical microstructure model is shown in Figure 20. The 2D mesh is regenerated in the GID tool to further reduce the computation cost.

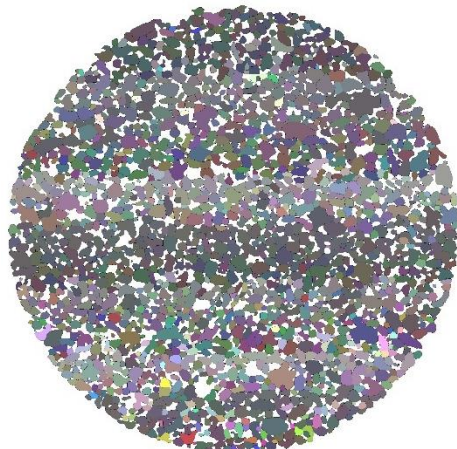


Figure 20. An example of the 2D numerical sandstone microstructure model



The SURE project has received funding from the European Union's Horizon 2020 research and innovation programme under grant agreement No 654662.

4.1.2.2 Construction of 3D sandstone microstructure model

The generation of the 3D volume mesh is performed using Avizo. In order to reduce the computation cost, the sample in Figure 19 is cut into a smaller sample with 5mm diameter and 2.5 mm thickness. The small sample has around 2600 grains with an average size of 0.2 mm. Since the surface mesh originally generated in the Avizo is normally very fine, it is firstly simplified before the generation of the volume mesh. The originally generated surface mesh and the simplified surface mesh with different number of faces are shown in Figure 21. It is computationally more expensive to retain the micropores.

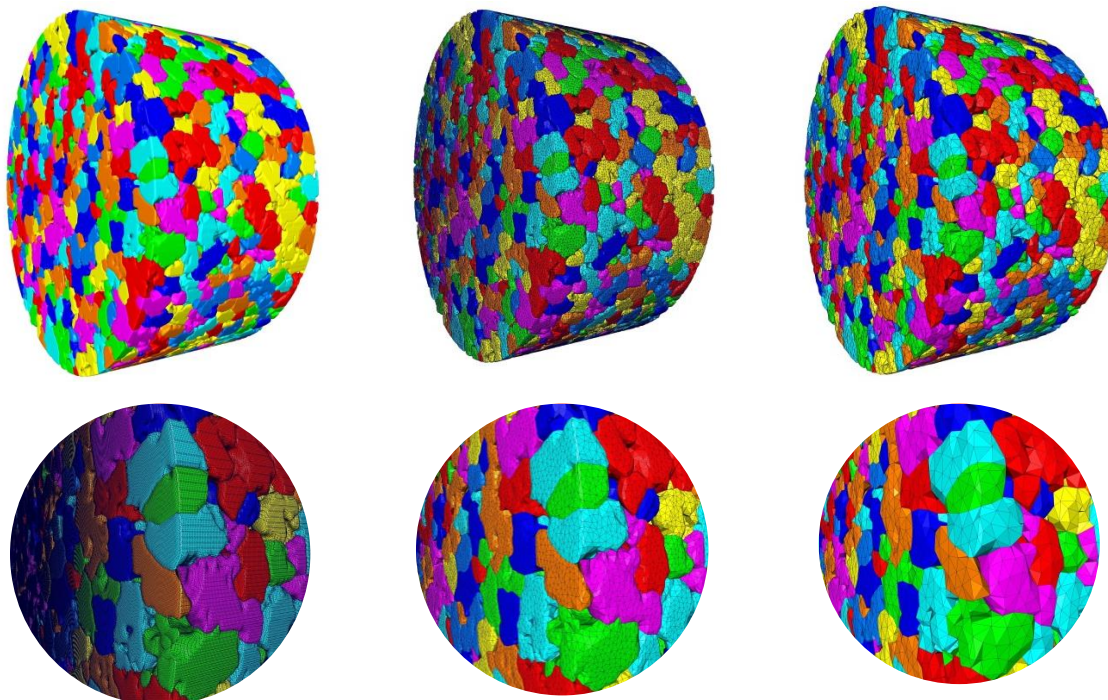


Figure 21. Surface mesh and close-up: original surface mesh with 44 million faces (left top); local enlargement (left bottom); simplified surface mesh with 1.5 million faces (middle top) and local enlargement (middle bottom); simplified surface mesh with 0.25 million faces (right top) and local enlargement (right bottom).

4.2 FDEM-GBM model for mechanical simulation of microstructure

4.2.1 Concept of the FDEM-GBM model

As shown in Figure 20 and Figure 21, the sandstone microstructure is well presented by grains discretised with triangular or tetrahedral elements. A reasonable approach for simulating the microscale mechanical behaviour of sandstone grains is to simulate the strong stiffness and strength inside the grain and the weaker joint or grain boundary strength behaviour between grains, which is the idea of the GBM (Potyondy, 2010) and is also a natural choice for the microscale model. Adopting this approach, the complex grain-scale interaction is expected to be simulated.

Different from the FDEM model for mesoscale simulation, two types of the joint elements are adopted for inter-grain and intra-grain element boundaries in the FDEM-GBM model. Two different sets of the parameters including elastic penalty number, tensile strength, cohesion,



The SURE project has received funding from the European Union's Horizon 2020 research and innovation programme under grant agreement No 654662.

energy release rate, etc. are used to present different stiffness and strength of the inter-grain and intra-grain joints. As shown in Figure 22, a weaker penalty number, tensile strength, etc are applied for the inter-grain joint model. For the inter-grain or intra-grain joints under tension, the stress increases with the tensile strain and starts to yield after the peak stress until eventually the joint is modelled as broken once a specific aperture is reached. A simple linear increase of the stress is modelled for the compression. For the joints under shear, the stress has a similar mode but ends up with a residual friction force. A symmetric response is expected for a reverse shear displacement.

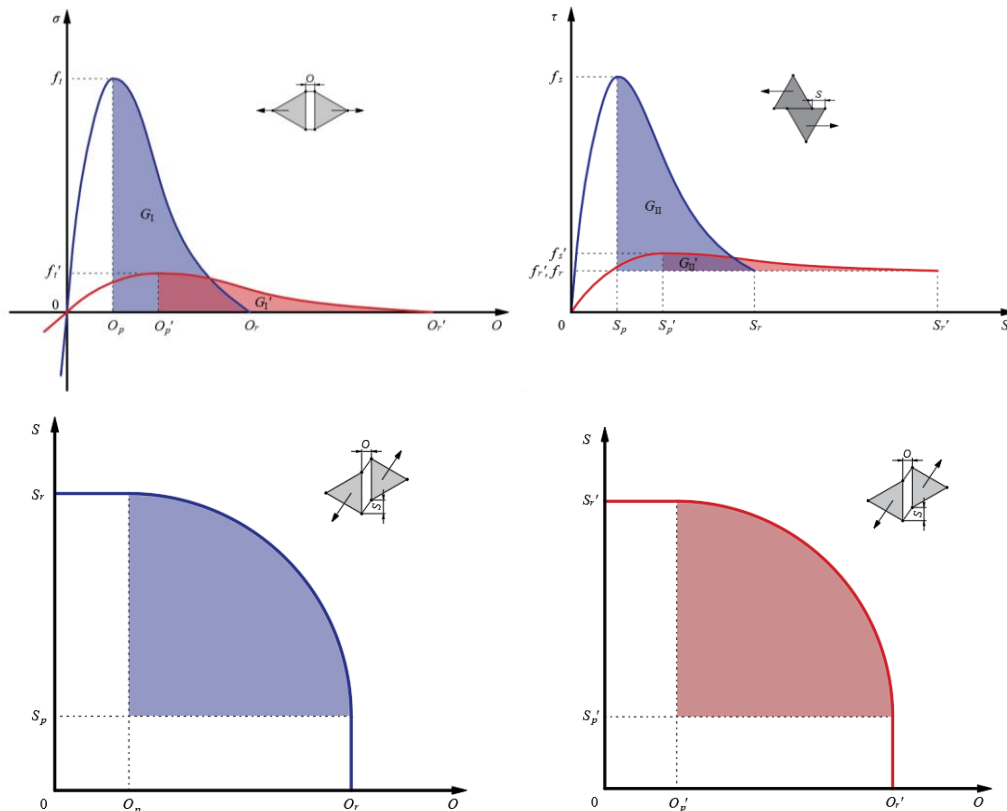


Figure 22. Inter-grain and intra grain joint model: stress-strain curve under tension for inter-grain (red) and intragrain (blue) joint (top left); stress-strain curve under shear for inter-grain (red) and intra-grain (blue) joint (top right); mixed-mode joint failure for intra-grain joint (bottom left) and mixed-mode joint failure for inter-grain joint (bottom right). O and S are the tensile and shear displacement; O_p and O_r are the joint opening at the peak stress and joint failure for intra-grain joints while O'_p and O'_r are the corresponding values for inter-grain joints. S_p and S_r are the joint shear displacement at the peak stress and joint failure for intra-grain joints while S'_p and S'_r are the corresponding values for inter-grain joints. f_t and f_s are the tensile and shear strength for the intra-grain joint while the f'_t and f'_s are the corresponding values for inter-grain joints. f_r and f'_r are the friction force between the two surfaces of the inter-grain or intra-grain joints and are set to be computed with the same friction coefficient.

4.2.2 Calibration of the numerical parameters

The numerical model is calibrated with the experimental Brazilian test results in this section. The input parameters for the numerical model include: 1) parameters for grain elements, density



The SURE project has received funding from the European Union's Horizon 2020 research and innovation programme under grant agreement No 654662.

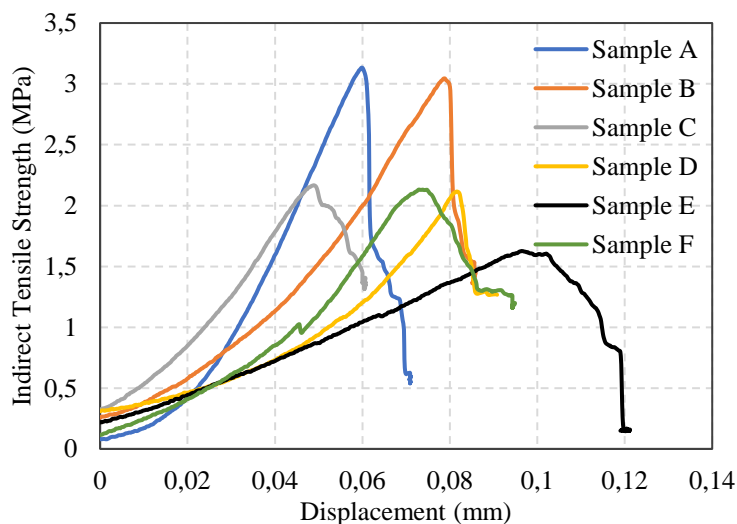
ρ , elastic modulus E and Poisson's ratio, ν ; 2) parameters for the elastic interaction between intra-grain or inter-grain elements, elastic penalty, k_n , contact penalty k_c ; 3) parameters related to the fracture model for intra-grain and inter-grain element boundaries, tensile strength f_t , internal friction coefficient k_μ , internal cohesion c , Mode I and Mode II fracture energy release rate G_I and G_{II} ; 4) mass damping coefficient μ . The experimental results are reported firstly and then the details about the numerical set-up are given and the model is calibrated with the experimental results.

4.2.2.1 Experimental setup and results

The geometries and the test results of the six sandstone samples are listed in Table 3. A relatively small sample size is used here considering the influence of the microstructure is believed to play a more important role on smaller scale loading conditions. The samples are tested using an in-house developed stiff loading frame as installed at the TU Delft rock mechanics laboratory, designed to handle a maximum load of 50 kN without significant apparatus compliance. Samples were deformed at a constant velocity of 20 $\mu\text{m/s}$, leading to sample failure on relatively short timescales as per ASTM standards. Load control was avoided such that the microstructure could be preserved. Diametral (line) load was measured with a load cell to an accuracy of 0.01 kN. Displacement was calculated by the average of two co-axially mounted Linear Variable Differential Transducers (LVDT) with an accuracy of 1 μm . Data was logged at 10 Hz such that ample data is available to allow precise comparison with numerically derived data. The loading force-displacement curves are shown in Figure 23 and vary considerably between different samples (1.6–3.2 MPa in indirect tensile strength) due to microscale heterogeneities and/or imperfections in sample dimensions from preparations. Individual measurement errors fall within the line thicknesses.

Table 3. Geometries of the six sandstone samples

Sample	A	B	C	D	E	F
Diameter (mm)	10.00	10.05	10.10	10.00	10.05	10.10
Thickness (mm)	6.85	5.45	5.70	4.90	6.00	5.60
Peak loading (kN)	0.337	0.328	0.233	0.228	0.175	0.229
Indirect tensile strength (MPa)	3.133	3.044	2.166	2.115	1.626	2.131



The SURE project has received funding from the European Union's Horizon 2020 research and innovation programme under grant agreement No 654662.

Figure 23. Brazilian test results of the sandstone samples

4.2.2.2 Numerical set-up

The numerical model set-up is shown in Figure 24. The two loading platens were placed closely to the specimen with no gap and were both assigned a constant velocity of 0.1 m/s towards the specimen. A sensitivity study of the loading velocity has also been conducted before the calibration. The time step should satisfy

$$\Delta t < \sqrt{\frac{V_{\min} \rho}{\max(E, k_n, k_c)}} \quad (11)$$

where V_{\min} is the minimum element volume in the simulation, ρ is the density, E , k_n and k_c are the elastic modulus, elastic penalty and contact penalty respectively.

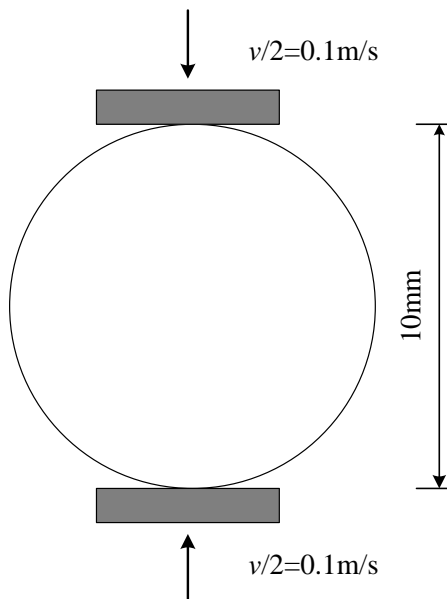


Figure 24. Numerical model set-up of Brazilian test

The 2D numerical microstructure model constructed from the CT-scan data of the Brazilian test sample No. 1 is used in the simulation and has been shown in Figure 20. The microstructure model has 69644 triangular elements and has a nominal size of 0.05 mm.

4.2.2.3 Determination of the numerical parameters

In this section the numerical parameters in the microstructure numerical model are calibrated with the experimental result for sample A. The element properties are determined according to the grain properties while the parameters governing the interaction between elements are divided into two groups: intra-grain element boundaries and inter-grain element boundaries. The triangular finite element grain properties are required to be those of the sandstone grains and the appropriate values are therefore those of quartz as listed in Table 3. Here, we shall adopt



The SURE project has received funding from the European Union's Horizon 2020 research and innovation programme under grant agreement No 654662.

quartz properties reported by Abdelaziz et al. (2018). Due to the lack of direct testing for the determination of inter-grain interaction properties, the corresponding parameters are calibrated to produce results consistent with experimental results.

The mesoscale or macroscale Young's modulus is determined by the grain stiffness and the joint stiffness between them. In the framework of the FDEM-GBM model, the grain stiffness is determined by the Young's modulus and the elastic penalty number for the intra-grain joints which are fixed. The stiffness of the inter-grain joint is determined by the elastic penalty number assigned to them. In order to investigate the relation between the mesoscale or macroscale Young's modulus and the inter-grain joint stiffness, a numerical uniaxial compression test (UCS) based on the 2D microscale model is set up (see Figure 25).

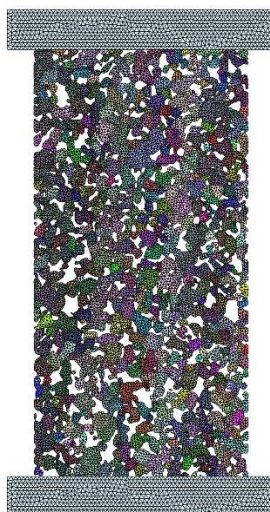


Figure 25. Numerical set-up of the uniaxial compression test (UCS)

As shown in Figure 25, the specimen is taken from the centre of the 2D microstructure model in Figure 20 and has a height of 8 mm and width of 4 mm. Two platens were placed on the top and bottom of the specimen and were assigned a constant velocity (0.0025 m/s) towards the specimen.

The elastic penalty number for the intra-grain joints is fixed to approximate the property of the grain to pure quartz and different values of the weakening coefficient (ratio between the elastic penalty number for intra-grain joint and elastic penalty number for inter-grain joints) are applied. The relation between the weakening coefficient and the numerical mesoscale (or macroscale) Young's modulus tested from the UCS is shown in Figure 26. As the weakening coefficient is increased, the effective Young's modulus of the sample decreases non-linearly.



The SURE project has received funding from the European Union's Horizon 2020 research and innovation programme under grant agreement No 654662.

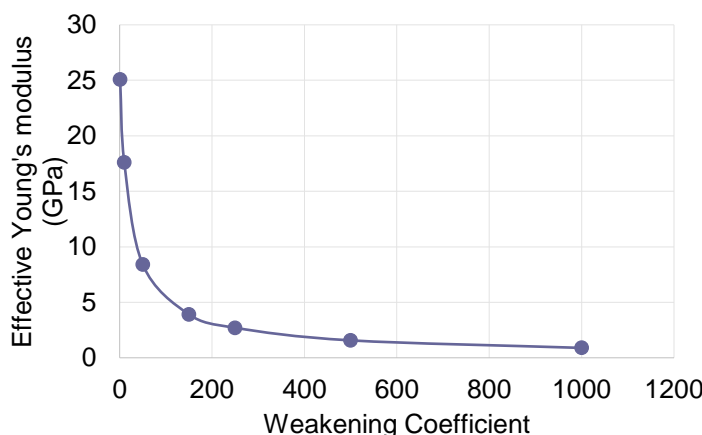


Figure 26. The effect of the weakening coefficient for elastic penalty number on the effective mesoscale or macroscale Young's modulus.

Since the experimental uniaxial compression test for the same sample is not available, the effective elastic Young's modulus of the sample is derived from the displacement-loading curve in the experimental Brazilian test in an indirect way. A quasi-static finite element analysis (FEA) of a mesoscale Brazilian test with the same geometry has been performed to derive the corresponding mesoscale elastic Young's modulus for sample A. As shown in Figure 27, the slope of the mesoscale simulation of the Brazilian test with 7.95 GPa elastic Young's modulus and 0.17 Poisson ratio matched with the slope of the experimental curve in the linear elastic stage quite well. The loading force in experiment has been transferred to the equivalent value for plain strain conditions to compare with the numerical result. But it needs to be noted that the numerical result is for a disc without any flattened edge on the top or bottom. There are two small flat edges on the top and bottom of the microscale model to keep the stability of the sample, which would slightly increase the stiffness of the sample. The weakening coefficient that best describes the experimental result is finally determined to be between 50 and 200 via trial and error.

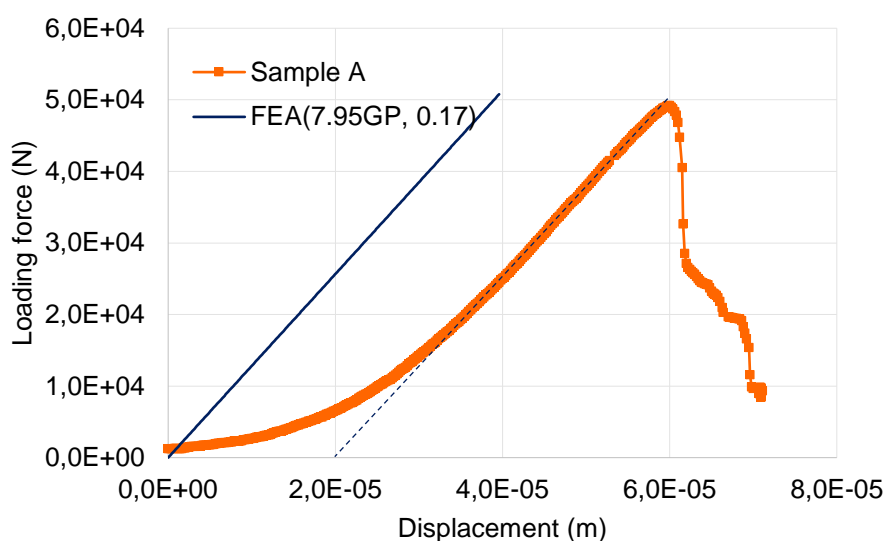


Figure 27 Comparison of the experiment result for sample A and quasi-static FEA result of mesoscale Brazilian test with the same geometry



The SURE project has received funding from the European Union's Horizon 2020 research and innovation programme under grant agreement No 654662.

The peak loading during the Brazilian test corresponds to the tensile failure of the rock in the central part of the sample. The mesoscale (or macroscale) intact tensile strength are determined by the tensile strength of the inter-grain and intra-grain joints. Here the tensile strength of the inter-grain joints is adjusted to match the peak loading in the numerical simulation with the experiment while the tensile strength of the intra-grain joints is fixed.

An ideal approach to determine the value of the inter-grain joint tensile strength with a specific intra-grain tensile strength is to do a parametric study to compute the corresponding mesoscale (or macroscale) tensile strength for different inter-grain joint tensile strengths and compare with the experimental results. Due to the lack of the direct tensile test results for this sandstone type, the tensile strength of the sandstone is estimated based on the indirect tensile strength from Brazilian test according to the empirical ratio. For the sedimentary rocks, the ratio of the direct tensile strength to the indirect (i.e. Brazilian disc test) tensile strength is around 0.68. Therefore, the mesoscale (or macroscale) direct tensile strength for the sample is about 2.13 MPa.

Theoretically, a direct shear test would help to determine the cohesion for the inter-grain joint. Here, the values of the weakening coefficient (ratio of intra- to inter-grain values) for the tensile strength and cohesion are kept the same.

The energy release rates (G_I and G_{II}) govern the energy consumed during crack propagation processes of yielding as shown in the stress-strain curve for the joints, which will also influence the peak load during the Brazilian test. The energy release rates are adjusted in our calibration simulations until the peak load in the numerical simulation matches the experimental results. The final parameters used in the numerical simulation are listed in Table 4.

Table 4. Input parameters of the 2D microscale simulation for Brazilian test calibrated with experimental results

Element properties	Values	
Bulk density, ρ (kg/m ³)	2700	
Young's modulus, E (GPa)	83.1	
Poisson's ratio, ν	0.17	
Mass damping coefficient, μ (Pa • s)	1	
Joint Properties	Intra-grain	Inter-grain
Elastic penalty, k_n (GPa)	415.5	2.77
Contact penalty, k_c (GPa)	415.5	2.77
Tensile strength, f_t (MPa)	48	12
Cohesion, c (MPa)	100	50
Internal friction coefficient, k_μ	1.27	1.27
Mode I energy release rate, G_I (J/m ²)	907	36.3
Mode II energy release rate, G_{II} (J/m ²)	1814	907

4.2.3 Model validation with experimental Brazilian test

4.2.3.1 Comparison of the fracture pattern in numerical simulation and experiment

In this section, the initiated fracture in the numerical Brazilian test is qualitatively compared with the experimental results. The numerical sample and CT-scan image before and after the Brazilian test are presented in Figure 28. As shown in the experimental result, the fracture



The SURE project has received funding from the European Union's Horizon 2020 research and innovation programme under grant agreement No 654662.

mostly propagated along the grain boundaries. Very rarely are grains broken during the test. The initiated fracture is almost in the centre of the sample. The numerical result is qualitatively consistent with the experimental result.

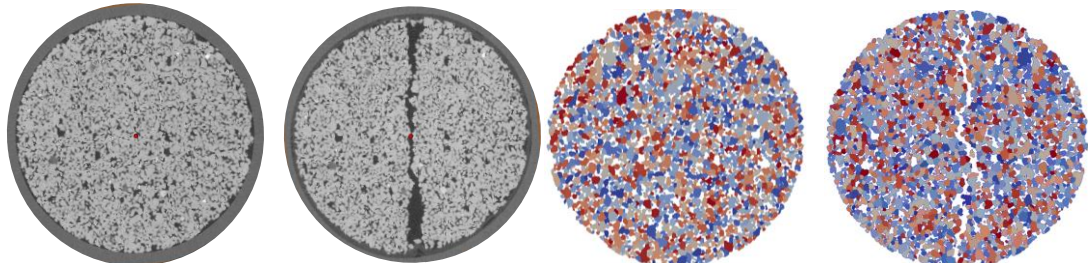


Figure 28. Comparison of the CT-scan image and numerical sample before and after Brazilian test (from left to right): CT-scan image before test; CT-scan image after test; numerical sample before test; numerical sample after test.

4.2.3.2 Comparison of the numerical and experimental load-displacement curve

The load-displacement curve in the numerical simulation is compared to the experimental load-displacement curve below. As shown in Figure 29, the slope and peak value for the numerical and experimental curves match each other well, which proves the microscale model and the corresponding calibrated parameters capture the mesoscale property quite well.

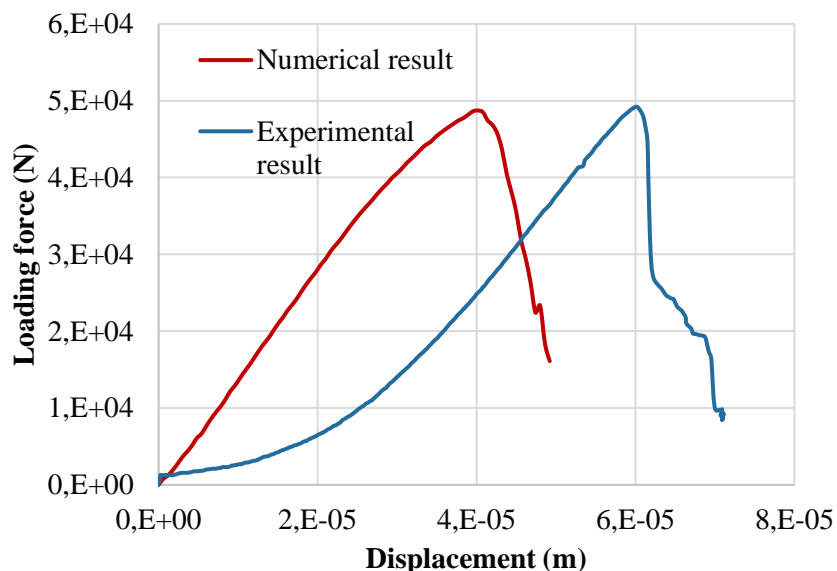


Figure 29 Comparison of the numerical and experimental load-displacement curve

4.2.3.3 Evolution of the minimum and maximum principle stress

To investigate the effect of the microstructure on the build-up of the stress in the sample, the maximum and minimum principle stresses are shown in Figure 30. With the movement of the platens, the stress inside the sample built up gradually. For the maximum principle stress, it mainly shows the compressive stress inside the sample. Due to the existence of the pores, the



The SURE project has received funding from the European Union's Horizon 2020 research and innovation programme under grant agreement No 654662.

platens are supported by an anastomosing network of stress chains that is seen in videos to fluctuate in path and intensity as yielding begins locally and then links up as the disc specimen fails. Similarly, the concentration of the tensile stress is also observed in a stress chain network, but mainly in the direction normal to the platen displacement direction. The high tensile stress emerges in the central part of the sample, which corresponds to the failure mechanism in the experiments. Once the disc is split in two, the left half can be seen to support the post-peak compressive load and the outer arc extensional stresses due to bending can be seen in the bottom right of Figure 30.

4.2.3.4 Discussion

2D simulation of pore and grain microstructural effects such as stress chain development gives strong insights into the realistic yielding mechanisms. But it is important to note that any comparison with experiments is limited by the fact that a real disc, however thin, will have several grains supporting the width of the specimen. However, the 2D representation in plane strain of a thin 3D disc specimen will be representing the microstructure as prismatically extruded microstructure in the third dimension. The consequence is likely to be that the numerical specimen's response to diametral loading will be even more dependent on the specimen's reference orientation with respect to the loading platen direction than would be the case for a disc specimen with real 3D microstructure. The variability of test results will be unrealistically high i.e. much will depend on which diametral points on the specimen are gripped. For this and other reasons, a more detailed calibration of inter- and intra-grain properties is reserved for use with 3D loading and 3D models, to be reported in future work.

Some grains which contact with each other in 3D might detach in 2D model, which in the worst case may result in some floating grains. The effect of the local defects such as big pores are also enlarged in the 2D model, which may lead to the underestimation of the sample strength. In addition, the imperfect shape of the 3D sample which is considered to have a link with the low slope of the loading-displacement curve in Brazilian test is not presented in the 2D model. Other reasons often cited for the low initial stiffness of the load displacement curve seen in experimental plots is the 'bedding-in' of equipment and its contacts with the potentially slightly displacing specimen at the start of loading.

The constitutive model of the intra-grain joint is kept identical with that for inter-grain joint but with different parameters. However, it can be imaged that the inter-grain contact might follow a nonlinear relation between the grain contact's aperture and contact force due to the surface roughness and filled cement between grains. For example, in the context of the compression, an increasing stiffness is expected with the increase of the contact area between the grain surfaces. The close of the initial aperture of the inter-grain contact zone is likely to contribute to an initially small but then increasing slope of the curve in the experiment. In addition, the strength of the inter-grain joint may also vary with the contact areas. Further experimental and numerical investigation is needed to propose a more accurate inter-grain joint model covering this non-linear load displacement behaviour.



The SURE project has received funding from the European Union's Horizon 2020 research and innovation programme under grant agreement No 654662.

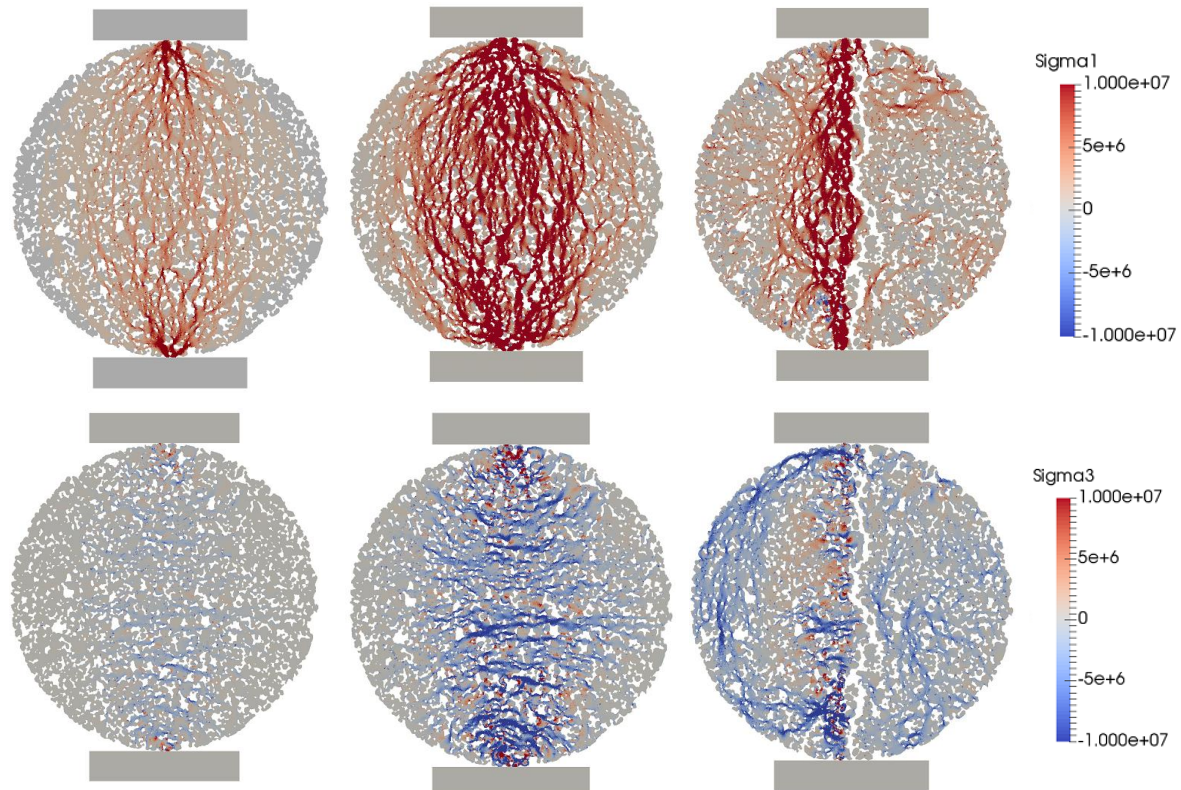


Figure 30 Contour of the minimum (bottom) and maximum (top) principle stress during the Brazilian test at resultant platen displacement: 5×10^{-3} mm (left), 2.5×10^{-3} mm (middle) and 5×10^{-2} mm (right).

4.3 Numerical simulation of water jet drilling including rock microstructure

4.3.1 Numerical simulation setup and material properties

The model setup is shown in Figure 31. The rock specimens are in the form of a squat cylinder with a diameter of about 10 mm and a thickness of 5 mm. The rock specimens are generated by a CT-scan based approach for constructing a sandstone microstructure model described in section 4.1.2. Figure 31 shows a sketch of a rock specimen with dimension and target zones for the high-pressure water jet to act on. The standoff distance between rock surface and nozzle outlet is 6 mm and the diameter of orifice is 2 mm. The exiting nozzle velocity magnitude varies from 0 m/s (nozzle wall) and 320 m/s (middle of nozzle), resulting in an average velocity of 160 m/s. We applied a zero gradient velocity boundary condition to the water outlet from the domain.



The SURE project has received funding from the European Union's Horizon 2020 research and innovation programme under grant agreement No 654662.

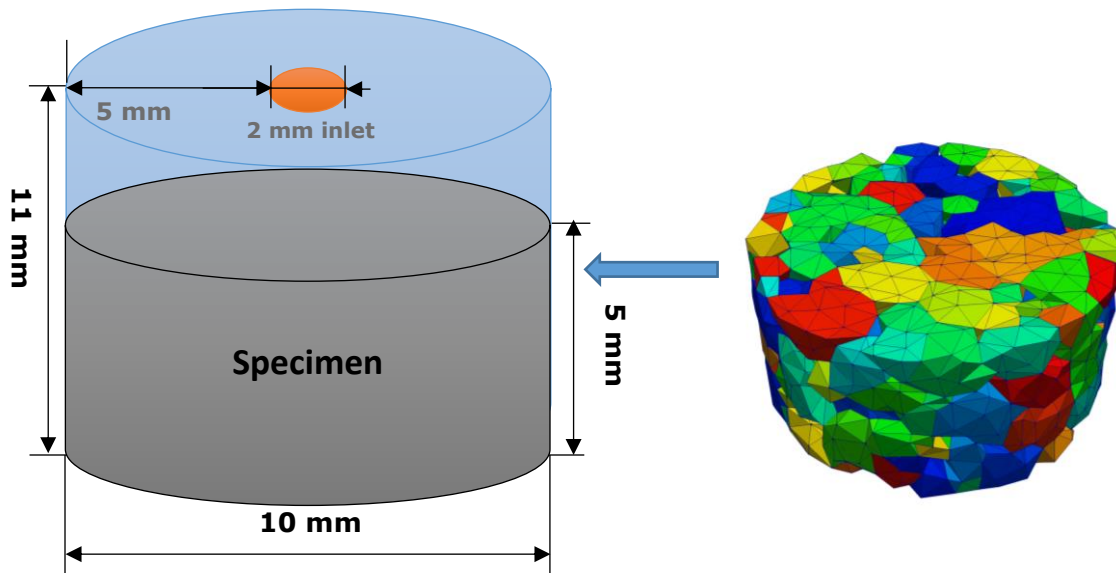


Figure 31 Sketch of simulation setup

Different from the setup of the material properties for mesoscale simulation, two types of joint elements are adopted for inter-grain and intra-grain element boundaries in the FDEM-GBM model at microscale. Two different sets of the parameters including, tensile strength and cohesion, are used to represent the different strengths of the inter-grain and intra-grain joints (Table 5 and 6). For these microscale model investigations, we only focus on one rock type, the Gildehaus Sandstone.

Table 5. Material properties for Intra-grain

Gildehaus	
Young's modulus E GPa	19.5
Poisson's ratio v	0.265
Bulk Density (kg/m ³)	2000
Tensile strength MPa	3.5
Internal friction angle	23
Cohesion MPa	17.5
UCS MPa	53
Gic J/m ²	8.2
Giic J/m ²	171.7

Table 6. Material properties for Inter-grain Joint

Gildehaus	
Tensile strength MPa	0.35
Internal friction angle	23
Cohesion MPa	1.75
Gic J/m ²	8.2
Giic J/m ²	171.7

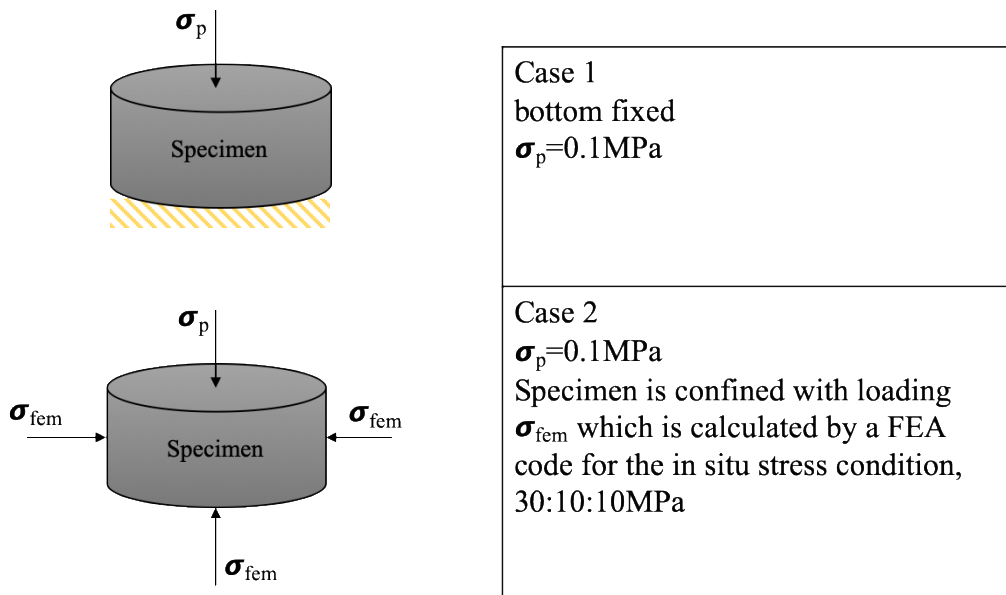


The SURE project has received funding from the European Union's Horizon 2020 research and innovation programme under grant agreement No 654662.

4.3.2 Boundary conditions

There are 2 test cases carried out at micro scale. Table 7 shows the boundary conditions of the simulations.

Table 7. Boundary condition of the simulations



4.3.3 Results and discussions

4.3.3.1 Case 1

The Gildehaus sandstone microstructure is well represented by grains reconstructed from CT-scan based approach. Grains are put into groups and each group is given a unique index (see Figure 32). As shown in Figure 32, the high speed water jet impacts on the specimen and spreads out. It is observed that several grains are ripped out from the left of the specimen and water flows out from beneath the lifted grains. This has not been observed in any numerical tests at meso-scale.

By cutting and slicing the specimen (see Figures 33 and 34), we found the specimen is highly heterogeneous. There are some quite big macro pores in the specimen. One of them is observed near the centroid of the specimen and highlighted by dashed lines in Figure 34b. Figure 33 shows water flow inside this pore and subsequently grains above the pore are lifted up and out.

After carefully analysing the results frame by frame, we found the pore is not connected by throat channels to the surface in the beginning (see Figure 34) even though it is only one grain above the pore. The grain of interest is to the side of the region directly hammered in compression in the jetting direction. This grain is much less confined than the grains directly under the hammer. The minimum principal stress component within the grain's elements and in inter-grain joint elements rapidly experience significantly high tensile stresses in excess of tensile strengths of grain boundaries. The rock specimen surface just outside the compressive hammer zone appears to go into tension and is broken into small fragments by the effect to the side of the high speed water jet. (In detail there are likely to be stress wave reflections causing transients tensile stresses but these cannot be resolved due to gaps between dump files). This



The SURE project has received funding from the European Union's Horizon 2020 research and innovation programme under grant agreement No 654662.

phenomenon that generates tensile stresses just beyond the direct water hammer zone can be identified as the “water hammer tensile mechanism”. After the grain is broken loose and into fragments, the water fluids then flow inside the pore. Note the suction pressures (blue) above the broken (blue) fragments after 75 μ s in Figure 34 (d) that may be contributing to the process. Water pressure rapidly builds within the now connected pore and targets one of the inter-grain boundaries that lies approximately parallel to the original surface that is opening and this is further prized open by fluid driven pressures. There therefore appears to be a combination of tensile spalling of a less confined free-surface that is then contributed to by fluid driven grain boundary opening and fluid entering neighbouring pores - leading to a bursting of pores near the surface surrounding the hammer head zone. This fluid driven phenomenon may be called “pore breakthrough”, i.e. water-driven grain interface breakthrough. Figure 35 shows most of cracks are tensile failure, only 12% are mixed mode failure.

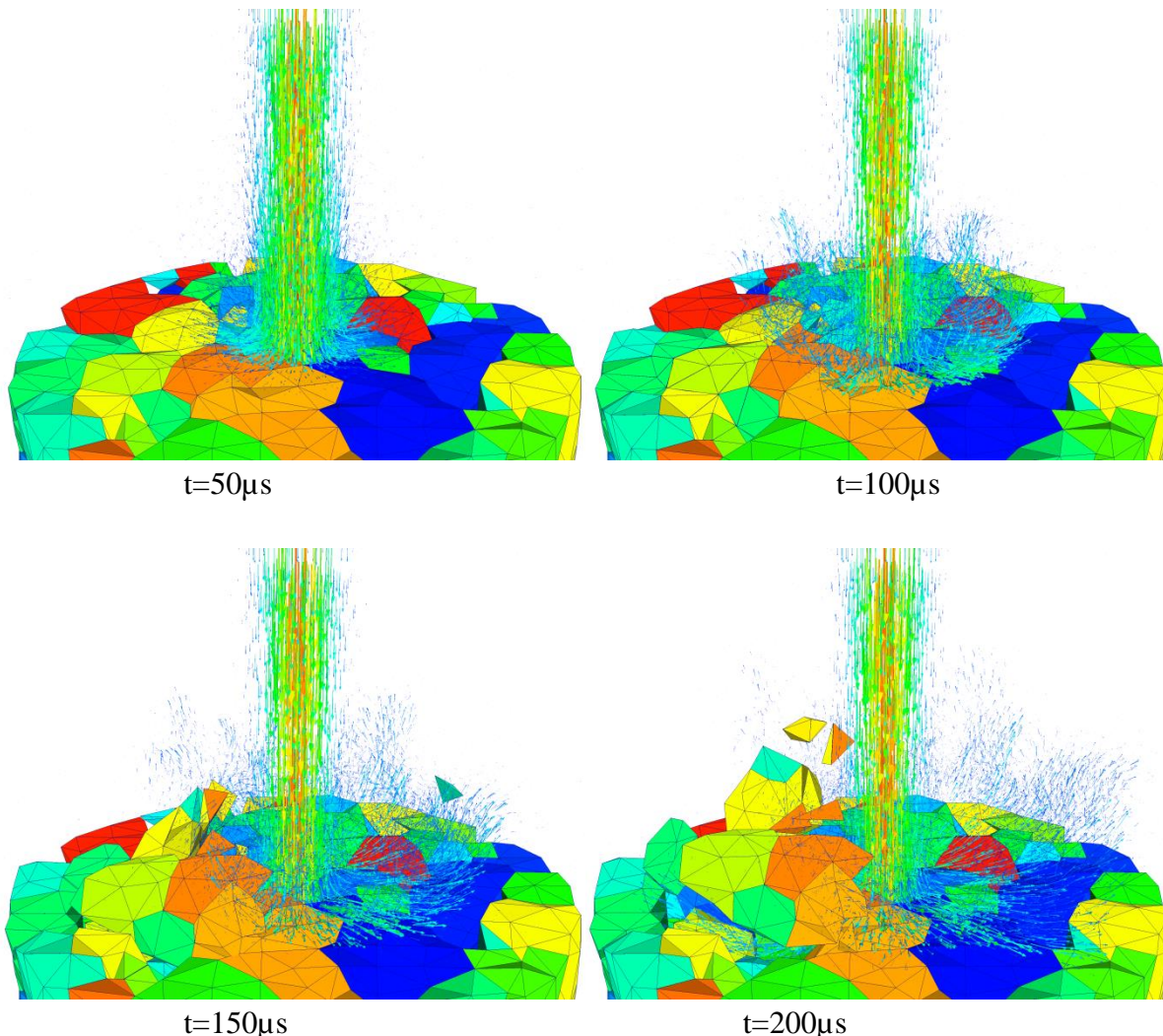


Figure 32. Water jet impact on specimen, micro grains are grouped and each group is given a unique index



The SURE project has received funding from the European Union’s Horizon 2020 research and innovation programme under grant agreement No 654662.

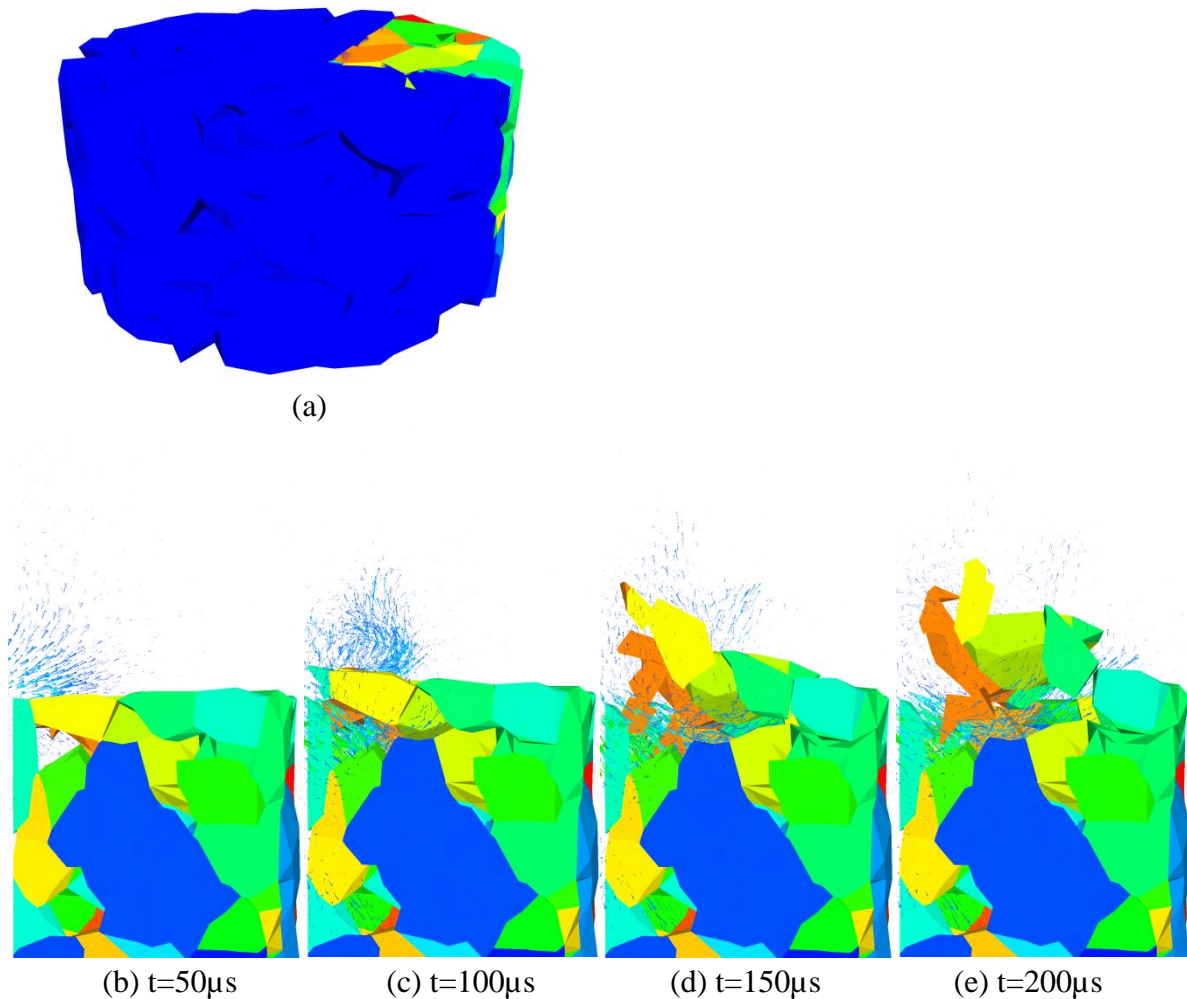


Figure 33. Specimen is clipped into a quarter of the cylinder highlighted in (a). b-c show the waters are flowing through the pore in the specimen, d-e show the breaking loose of fragments as they are carried off in suspension.



The SURE project has received funding from the European Union's Horizon 2020 research and innovation programme under grant agreement No 654662.

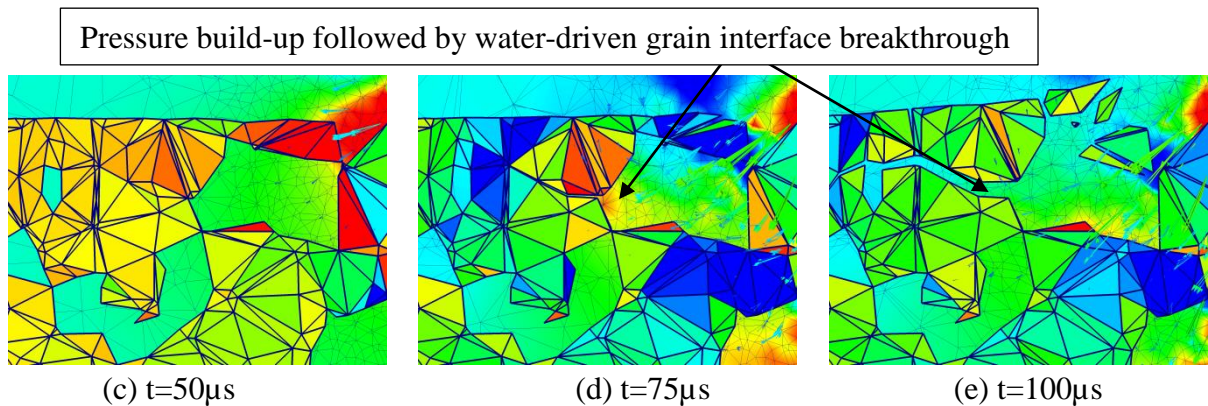
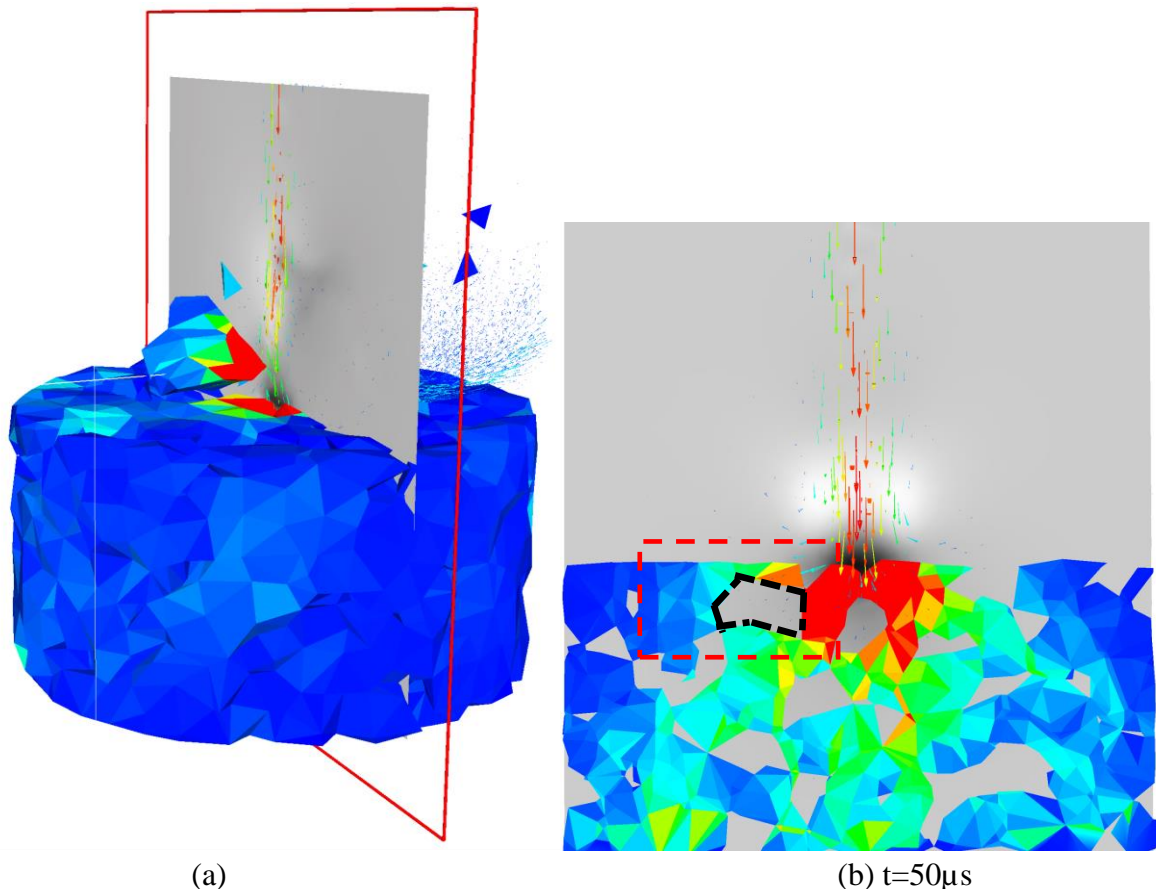


Figure 34. The cross section of the specimen shows up the highly heterogeneous stress state in the specimen. (a-b) indicate σ_3 magnitudes as red colours indicating σ_3 becomes significantly tensile and sufficient for failure, (c)-(e) show zoom in cross-section highlighted in (b): solid meshes are represented by bold meshes (note the mesh shapes look poor quality but are not as these are projections of 3D meshes onto a 2D cut plane), hot colour shows σ_3 is tension; fluid meshes are represented by thin meshes and a finer mesh size can be seen in pores with flow and pressure gradients, colour outside solid represents fluid pressure field.



The SURE project has received funding from the European Union's Horizon 2020 research and innovation programme under grant agreement No 654662.

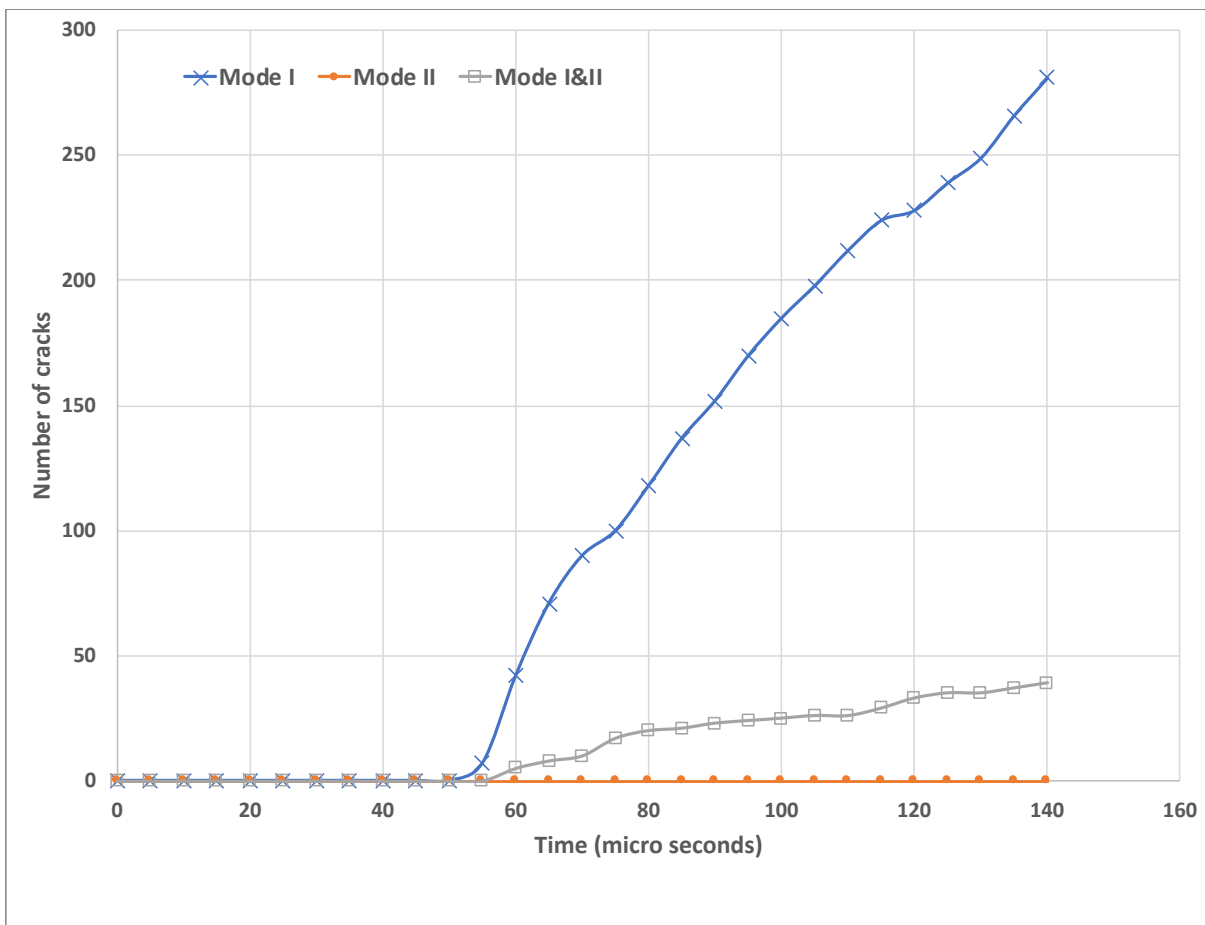


Figure 35. Numbers of cracks in different failure mode vs time

4.3.3.2 Case 2

In this case, the specimen is confined by loading σ_{fem} which is calculated by a FEA code for the true triaxial in-situ stress far field boundary condition, 30:10:10 MPa (across hole horizontal max: across hole horizontal min: axial jetting direction). The procedure for calculating the loading boundary conditions near the hole is described in report D 7.2. Under this boundary condition, the specimen is under lateral compression with a stress ratio across the jetting direction and significant additional axial compression. Fewer joint elements are in tension and reach the criterion of tensile failure. Therefore, this subsurface in-situ stress condition will be associated with a reduced the jet-ability. As shown in Figure 36, only one big grain is ripped out of the specimen which is similar to the Case 1 result. A similar flow pattern is observed in this case (see Figure 37). Comparing with Case 1 with 280 Mode 1 and 40 Mixed Mode cracks by 140 μ s, fewer cracks/fragments are generated for Case 2 – only 28 (M1) and 16 (MM) cracks. The proportion of cracks in mixed mode failure increases from 12% to 39% in Case 2. It is concluded that the confinement of in-situ stress has a very significant effect on ‘jet-ability’ of RJD. The results are in good agreement with experimental results that report increases in back pressure generally inhibit jet-ability (Hahn et al., 2019).



The SURE project has received funding from the European Union’s Horizon 2020 research and innovation programme under grant agreement No 654662.

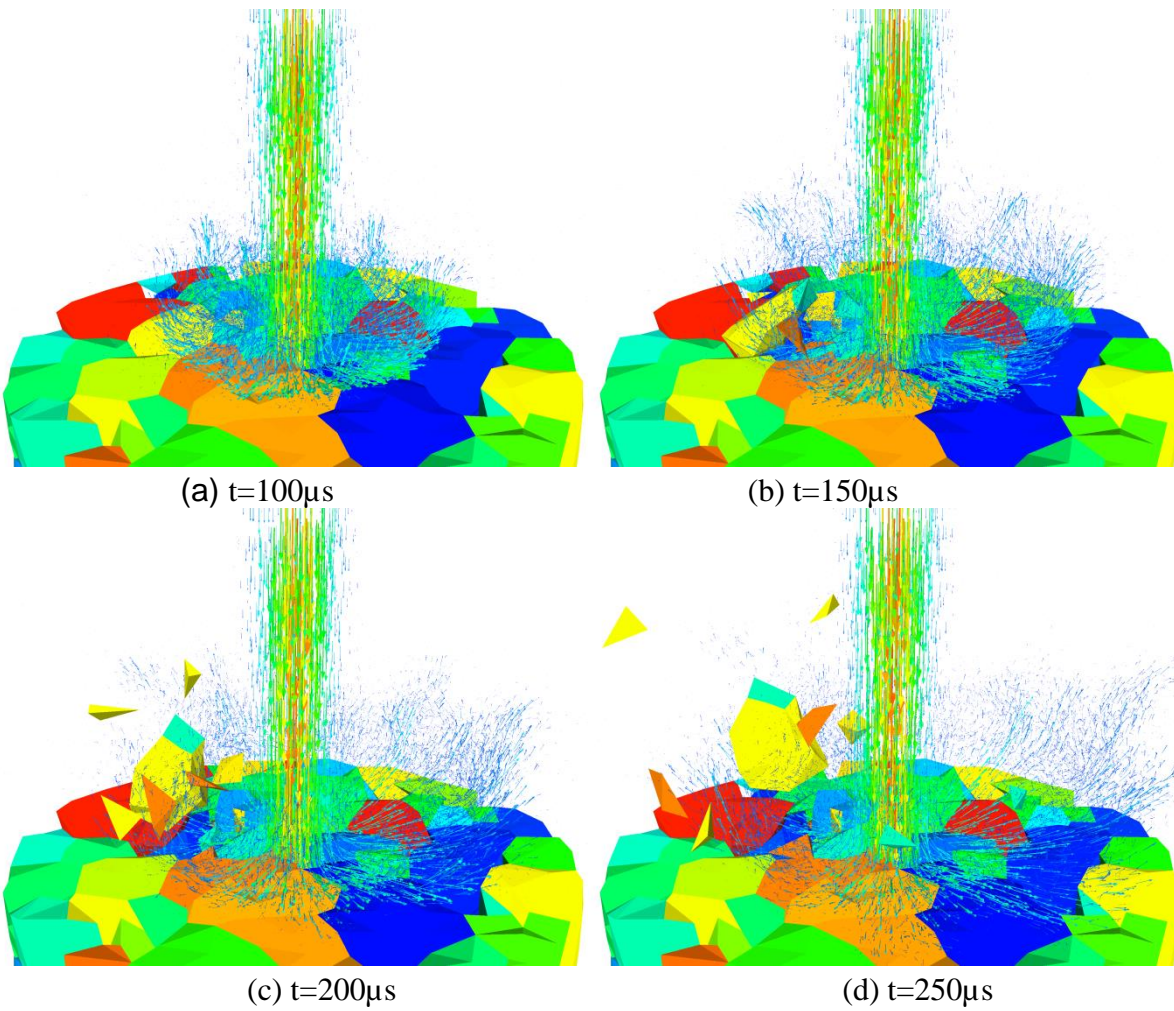


Figure 36 Water jet impact on specimen, micro-grains are typically quartz grains of the sandstone and are sometimes grouped - each group is given a unique index (a separate colour)

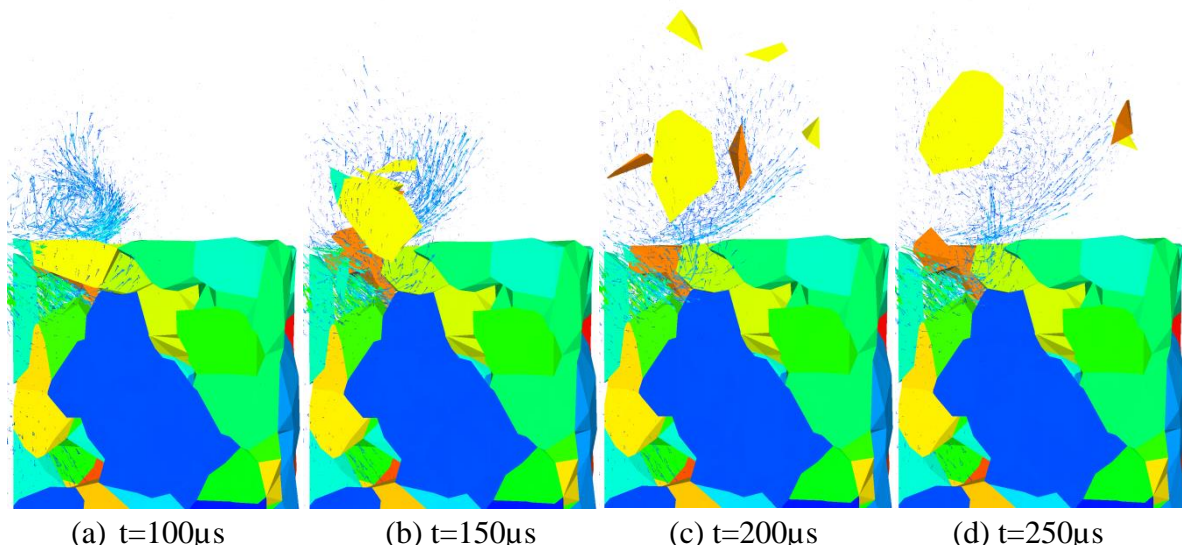


Figure 37. Specimen is clipped into a quarter of cylinder. The water is flowing through some of the pores in the specimen.



The SURE project has received funding from the European Union's Horizon 2020 research and innovation programme under grant agreement No 654662.

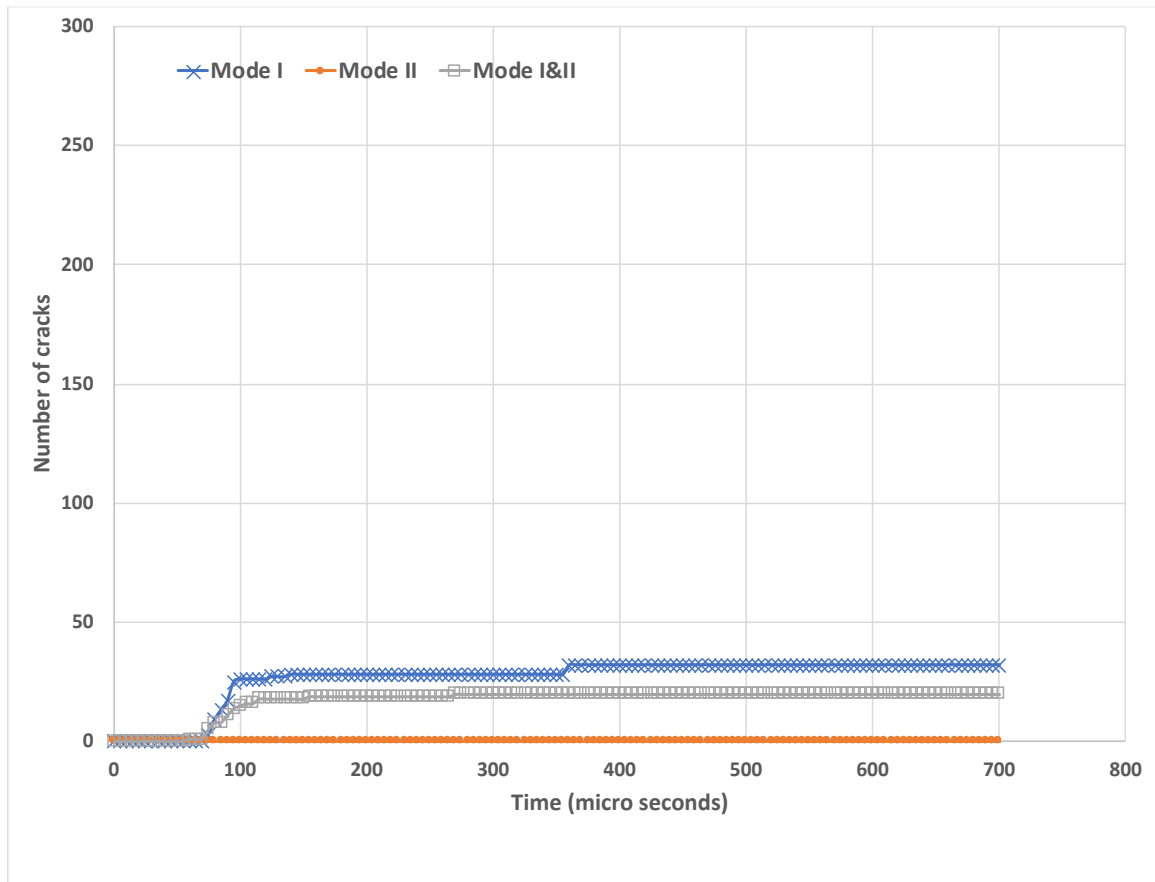


Figure 38. Case 2: Confined triaxial in-situ stress. Numbers of cracks in different failure mode vs time (far fewer than in Case 1)

4.3.3.3 Discussion

Although the first crack in the simulation in Case 1 was a radial crack forming directly beneath the water hammer in the direction of the jet, the higher confinement and normal stress across it suppressed its opening. The damage mechanisms for very porous sandstone described as hammer action followed by pore breakthrough were revealed very effectively (Figure 34) in the micro-structural model with low confinement (Case 1). These mechanisms were also seen but to less destructive effect in Case 2. Case 2 was an attempt to reproduce the jetting under true triaxial test conditions investigated by Hahn and Bakker in TU Delft (Hahn et al., 2017). However, the establishment of a significant amount of jet-hole depth and advancing nozzle would be necessary for the boundary conditions of the numerical simulations to be comparable to laboratory jetting action that extends the jet-hole depth and takes away fragments in the returning annulus. So far in this work, the hammer action mechanism leading to tensile (and mixed mode) cracks has been established as potentially the most important for breakdown of strong rock types other than sandstones, rocks that may have low to negligible porosity. To maximise this, high frequency high intensity pulse delivery should remain a target of research into jet-drilling and related drilling stimulation methods for geothermal energy, as concluded in D5.4 (Gradzki et al., 2019). As jet-assisted drilling simulation research with micro-structure turns to rocks like granite, the repeated hammer effect may drive another mechanism. If granite is to be jetted, the jetting will need to exploit weaknesses and possibly cyclic fatigue on grain



The SURE project has received funding from the European Union's Horizon 2020 research and innovation programme under grant agreement No 654662.

boundaries. In such a case the mismatching deformational responses of neighbouring mineral phase to hammer stressing and de-stressing would seem to be a key target for investigation of a jet-drill and its advancing breakage and fragment removal. This mechanism is also within the scope of the numerical modelling methodologies developed in this research project. Under high confinement with greater reservoir depths, the harnessing of the assistance of shear failure and excavation caving in high compressive differential stresses becomes an important consideration to supplement the progressively more suppressed-with-depth tensile failure mechanisms.

5 Conclusions

A new 3D immersed body method in which the fracture model was incorporated into a two-way fluid-solid coupling model is proposed. To investigate the effect of the water pore pressure, Biot's theory was implemented. The new fluid-solid coupling model with the 3D fracture model is capable of simulating crack initiation, propagation and fragment removal under the impact load of a high-speed water jet. Under the condition of average water exiting velocity of 160 m/s and standoff distance 6 mm, and atmospheric conditions, Gildehaus sandstone represented by a smooth target surface can be cracked and subsequently eroded under water jet impact while Dortmund sandstone, and Icelandic Basalt are harder to be broken out and eroded, which qualitatively agrees with experimental observations from Deliverable 5.1 (Hahn et al. 2017). For Gildehaus sandstone, the main drilling mechanism is identified as "water hammer effect" which we now associate with dominantly tensile failures. The numerical results show most of cracks are pure tensile failure, only 20% of cracks are mixed mode failure and none are pure shear mode.

For transient effects of the pore water pressure for Gildehaus sandstone, it is found that after considering pore pressure transient changes due to the jet pulse arriving, RJD generates cracks in slightly wider areas than when using a theory that ignores pore pressure transients in the rock. The result demonstrates that the transient effect under the hammer leads to an elevated pore pressure which will act to enhance the RJD "jet-ability" but not very significantly. The effect of the pore pressure transients arriving and spreading from under the hammer head only slightly enhances the shear failures in Case 4 for which the sample is under a radial confining stress of 5 MPa and back pressure of 0.1 MPa. When the back pressure is increased from 0.1 MPa to 2.5 MPa under the same constraint conditions (5 MPa radially on side wall surfaces), the cracking and jet penetration of rock is significantly reduced.

The numerical tests presented in this report show good agreement with experimental results qualitatively. It is worth mentioning that more quantitative benchmark tests, e.g. based on true triaxial compression boundary conditions with in-situ pore-pressure, need to be performed to validate this model.

To investigate the influence of the rock microstructure on the water jet drilling, the sandstone microstructure must first be constructed and the related influence on the rock failure can then be investigated. In this work the rock microstructure and its failure mechanism was first investigated in the context of the Brazilian test and as a solids-only problem. The proposed workflow from CT-scan data to grain-scale simulation of rock failure is a significant advance on previous work for investigating related problems where the rock microstructure plays an important role. These main contributions of solids-only behaviour are pre-requisites to the further coupled modelling of fluid jet interactions with micro-structural representations of sandstone (and other rock types) and these are summarized as the following two important



The SURE project has received funding from the European Union's Horizon 2020 research and innovation programme under grant agreement No 654662.

developments. First, a novel approach for constructing the rock microstructure model based on CT-scan data is implemented. The approach starts from the real CT-scan imaging data from which is constructed the geometry and then the numerical mesh to target a numerical replica of the original cored rock fabric. A compromise between the model accuracy and the element numbers used is reached. The actual microstructure information from the CT-scan data is retained as much as is deemed possible under a specific limitation of computation cost. The cost in terms of extended run-times requires a certain degree of modelling experience that was ascertained in this study. Second, with the microstructure model now constructed, microscale failure mechanisms of a porous sandstone during indirect tensile Brazilian testing is investigated with the new FDEM-GBM model. The numerical parameters in the FDEM-GBM model were firstly calibrated with experimental results from specimens of the sandstone. A sensitivity study was performed to investigate the effect of the inter-grain microstructure property on the mesoscale rock property and to find out a reasonable value to assign to further simulation of brittle failure in this sandstone. Eventually, the separation and shear displacement of the sandstone grains was illustrated in the simulated indirect tensile failure conditions of the Brazilian test. The corresponding grain-scale failure mechanisms that were simulated were also compared to those of the CT-scan data of the failed Brazilian test laboratory samples, showing a very close match of grain scale breakage mechanisms.

The currently reported solids-only work is still limited to 2D due to the high computation cost and considerable number of tests required during the parameter calibration for 3D. The differences between the 2D and 3D microstructural models are easily anticipated. Most notably, the heterogeneity is enlarged in the 2D case.

The microscale simulation of water jet drilling is carried out using the same method as in the mesoscale model but considering the rock microstructure heterogeneity. The microscale simulation of water jet drilling demonstrates two jet drilling erosion mechanisms: (a) ‘water hammer effect’ suggesting shock waves (elevated stress levels) for breaking apart weak inter-grain joints mainly by tensile failure; (b) ‘pore breakthrough effect’ where water gains access to a pore and the elevated pressure inside is driven between weaker grain interfaces causing pore breakthrough. Water flowing inside the macro-pores opens the weaker inter-grain boundary cracks and fragments the structures surrounding the macro-pores. The numerical results confirm that for such porous sandstone as this Gildehaus sandstone (20-25%), as inter-grain tensile strength and cohesion of grain boundaries are assigned weaker values, the jet-ability is enhanced. The particular jetting simulation case of in-situ stress confinement and high far field stress ratio (3:1) across the block (30:10:10 MPa) decreases the jet-ability significantly when compared with the unconfined jetting conditions that were also simulated. Due to high CPU cost, the current work is limited to simulate a small domain for a short transient (<1 ms). However, after it is fully optimised and parallelised, we expect that this coupled model will be able to simulate larger domains over longer jetting periods including a jetting sequence of multiple short pulses to examine the promising process of high intensity stress cycling with water hammer effect. It is within the scope of the solid-fluid coupled methodology to extend the current microstructure method to include abrasive charged jets, rotating nozzles and hybrid percussion or rotary tools in addition to the water jetting actions.

6 Acknowledgements

The SURE project has received funding from the European Union’s Horizon 2020 research and innovation programme under grant agreement No 654662. The content of this report reflects



The SURE project has received funding from the European Union’s Horizon 2020 research and innovation programme under grant agreement No 654662.

only the authors' view. The use of X-Ray CT data from true triaxial jetting tests undertaken at TU Delft, by Richard Bakker and Simon Hahn (GZB) and Richard Bakker's sharing of data on small Brazilian disc tests is gratefully acknowledged.

7 References

- Abdelaziz, A., Q. Zhao, and G. Grasselli. 2018. Grain based modelling of rocks using the combined finite-discrete element method. *Computers and Geotechnics*, 103, 73-81.
- Chen, S., Z. Q. Yue, and L. G. Tham. 2004. Digital image-based numerical modeling method for prediction of inhomogeneous rock failure. *International Journal of Rock Mechanics and Mining Sciences*, 41(6), 939-957.
- Chen, S., Z. Q. Yue, and L. G. Tham. 2006. Digital Image Based Approach for Three-Dimensional Mechanical Analysis of Heterogeneous Rocks. *Rock Mechanics and Rock Engineering*, 40(2), 145-168.
- CIMNE, 2019. GID 14.0 User Manual.
<https://www.gidhome.com/documents/usermanual/en/Tabla%20de%20Contenidos>
- Dehkhoda, S., Hood, M. An experimental study of surface and sub-surface damage in pulsed water-jet breakage of rocks. *Int. J. Rock Mech. Min. Sci.* **2013**, 63, 138–147.
- Detournay, E., A.H.-D.Cheng, 1988, Poroelastic response of a borehole in a non-hydrostatic stress field, International Journal of Rock Mechanics and Mining Sciences & Geomechanics Abstracts, Volume 25, Issue 3, Pages 171-182
- Gao, F., and H. Kang. 2017. Grain-Based Discrete-Element Modeling Study on the Effects of Cementation on the Mechanical Behavior of Low-Porosity Brittle Rocks. *International Journal of Geomechanics*, 17(9), 04017061.
- Gao, F., D. Stead, and D. Elmo. 2016. Numerical simulation of microstructure of brittle rock using a grain-breakable distinct element grain-based model. *Computers and Geotechnics*, 78, 203-217.
- Ghazvinian, E., M. S. Diederichs, and R. Quey. 2014. 3D random Voronoi grain-based models for simulation of brittle rock damage and fabric-guided micro-fracturing. *Journal of Rock Mechanics and Geotechnical Engineering*, 6(6), 506-521.
- Gradzki, Daniel P., Niklas Geißler, Jascha Börner, Viktor Hartung, Simon Hahn, Volker Wittig: Deliverable 5.4: Report on Novel Water Jet Drilling Tool; Potsdam: GFZ German Research Centre for Geosciences, DOI 10.2312/GFZ.4.8.2019.012
- Gui, Y. L., Z. Y. Zhao, J. Ji, X. M. Wang, K. P. Zhou, and S. Q. Ma. 2016. The grain effect of intact rock modelling using discrete element method with Voronoi grains. *Géotechnique Letters*, 6(2), 136-143.
- Guo, L. 2014. Development of a three-dimensional fracture model for the combined finite-discrete element method. PhD thesis, Imperial College London.
- Hahn, S. Wittig, V. Jasper, S.,Schwarz, D, Albadroui D , Hoogland, K, R. Bakker R. R. 2019. Deliverable 5.2: Report on Jet drilling at simulated reservoir conditions; Potsdam : GFZ German Research Centre for Geosciences, DOI:10.2312/gfz.4.8.2019.002Jiang, H., C. Du, S. Gao, K. Liu, 2014, Numerical simulation of rock fragmentation under the impact load of water jet, Shock and Vibration Volume 2014, Article ID 219489, 11 pages
- Lesueur, M., M. C. Casadiego, M. Veveakis, and T. Poulet. 2017. Modelling fluid-microstructure interaction on elasto-visco-plastic digital rocks. *Geomechanics for Energy and the Environment*, 12, 1-13.



The SURE project has received funding from the European Union's Horizon 2020 research and innovation programme under grant agreement No 654662.

- Li, C.-S., D. Zhang, S.-S. Du, and B. Shi. 2016. Computed tomography based numerical simulation for triaxial test of soil–rock mixture. *Computers and Geotechnics*, 73, 179-188.
- Li, J., H. Konietzky, and T. Frühwirt. 2017a. Voronoi-Based DEM Simulation Approach for Sandstone Considering Grain Structure and Pore Size. *Rock Mechanics and Rock Engineering*, 50(10), 2749-2761.
- Li, X., Z. Liu, S. Cui, C. Luo, C. Li, and Z. Zhuang. 2019. Predicting the effective mechanical property of heterogeneous materials by image based modeling and deep learning. *Computer Methods in Applied Mechanics and Engineering*, 347, 735-753.
- Li, X. F., H. B. Li, and J. Zhao. 2017b. 3D polycrystalline discrete element method (3PDEM) for simulation of crack initiation and propagation in granular rock. *Computers and Geotechnics*, 90, 96-112.
- Lisjak, A., O. K. Mahabadi, L. He, B. S. A. Tatone, P. Kaifosh, S. A. Haque, and G. Grasselli. 2018. Acceleration of a 2D/3D finite-discrete element code for geomechanical simulations using General Purpose GPU computing. *Computers and Geotechnics*, 100, 84-96.
- Liu, Q., Y. Jiang, Z. Wu, and J. He. 2018. A Voronoi element based-numerical manifold method (VE-NMM) for investigating micro/macro-mechanical properties of intact rocks. *Engineering Fracture Mechanics*, 199, 71-85.
- Liu, X., S., Liu and H. Ji, 2015, Numerical research on rock breaking performance of water jet based on SPH, Powder Technology, Volume 286, December 2015, Pages 181-192)
- Lu, Y.Y., Huang, F., Liu, X.C., Ao, X. On the failure pattern of sandstone impacted by high-velocity water jet. *Int. J. Impact Eng.* 2015, 76, 67–74.
- Ma, G., W. Zhou, R. A. Regueiro, Q. Wang, and X. Chang. 2017. Modeling the fragmentation of rock grains using computed tomography and combined FDEM. *Powder Technology*, 308, 388-397.
- Mahabadi, O. K., B. S. A. Tatone, and G. Grasselli. 2014. Influence of microscale heterogeneity and microstructure on the tensile behavior of crystalline rocks. *Journal of Geophysical Research: Solid Earth*, 119(7), 5324-5341.
- Munjiza, A., 2004, The combined finite-discrete element method. John Wiley & Sons.
- Obeysekara, A. I. B. 2018. Numerical Modelling of Fluid-Driven Fracturing in Naturally Fractured Rock, PhD thesis, Imperial College London.
- Pain, C., M. Piggott, A. Goddard, F. Fang, G. Gorman, D. Marshall, M. Eaton, P. Power, and C. De Oliveira, 2005, Three-dimensional unstructured mesh ocean modelling. *Ocean Modelling*, 10(1):5–33.
- Pain, C., A. Umpleby, C. De Oliveira, and A. Goddard. 2001, Tetrahedral mesh optimisation and adaptivity for steady-state and transient finite element calculations. *Computer Methods in Applied Mechanics and Engineering*, 190(29):3771–3796.
- Peng, J., L. N. Y. Wong, and C. I. Teh. 2017. Influence of grain size heterogeneity on strength and microcracking behavior of crystalline rocks. *Journal of Geophysical Research: Solid Earth*, 122(2), 1054-1073.
- Piggott, M., P. Farrell, C. Wilson, G. Gorman, and C. Pain, 2009, Anisotropic mesh adaptivity for multi-scale ocean modelling. *Philosophical Transactions of the Royal Society of London A: Mathematical, Physical and Engineering Sciences*, 367(1907):4591–4611.
- Polanskey, C.A., Ahrens, T.J. 1990. Impact spallation experiments: fracture patterns and spall velocities. *Icarus*., 87, 140–155.



The SURE project has received funding from the European Union's Horizon 2020 research and innovation programme under grant agreement No 654662.

- Potyondy, D. O. 2010, *A Grain-Based Model for Rock: Approaching the True Microstructure*. Paper presented at the Rock Mechanics in the Nordic Countries 2010, Kongsberg, Norway. (June 9-12, 2010).
- Reinsch, T., B. Paap, S. Hahn, V. Wittig, and S. van den Berg, 2018, Insights Into the Radial Water Jet Drilling Technology - Application in a Quarry, *Journal of Rock Mechanics and Geotechnical Engineering*, Vol. 10(4)
- Sakaguchi, K., Y. Yumoto, A. Kizaki, 2013, Numerical simulation of the water jet excavation of soft rock saturated with water, *ISRM International Symposium - EUROCK 2013*, 23-26 October, Wroclaw
- Suchorzewski, J., J. Tejchman, and M. Nitka. 2018. Experimental and numerical investigations of concrete behaviour at meso-level during quasi-static splitting tension. *Theoretical and Applied Fracture Mechanics*, 96, 720-739.
- Tan, X., H. Konietzky, and W. Chen. 2016. Numerical Simulation of Heterogeneous Rock Using Discrete Element Model Based on Digital Image Processing. *Rock Mechanics and Rock Engineering*, 49(12), 4957-4964.
- Tatone, B. S. A., and G. Grasselli. 2015. A calibration procedure for two-dimensional laboratory-scale hybrid finite-discrete element simulations. *International Journal of Rock Mechanics and Mining Sciences*, 75, 56-72.
- Vire', J. Xiang, F. Milthaler, P. E. Farrell, M. D. Piggott, J.-P. Latham, D. Pavlidis, and C. C. Pain, 2012, Modelling of fluid–solid interactions using an adaptive mesh fluid model coupled with a combined finite–discrete element model. *Ocean Dynamics*, 62(10-12):1487–1501, 2012.
- Vire', J. Xiang, and C. Pain, 2015, An immersed-shell method for modelling fluid–structure interactions. *Philosophical Transactions of the Royal Society of London A: Mathematical, Physical and Engineering Sciences*, 373(2035):20140085.
- Xiang, J., A. Munjiza, and J.-P. Latham, 2009, Finite strain, finite rotation quadratic tetrahedral element for the combined finite–discrete element method. *International Journal for Numerical Methods in Engineering*, 79(8):946–978.
- Yang, J. and E. Balaras., 2006, An embedded-boundary formulation for large-eddy simulation of turbulent flows interacting with moving boundaries. *Journal of Computational Physics*, 215(1):12–40.
- Yang, P., J. Xiang, M. Chen, F. Fang, D. Pavlidis, J.-P. Latham, and C. Pain, 2017, The immersed-body gas-solid interaction model for blast analysis in fractured solid media. *International Journal of Rock Mechanics and Mining Sciences*, 91:119–132.
- Yang, P., J. Xiang, F. Fang, D. Pavlidis, J.-P. Latham, and C. Pain, 2016, Modelling of fluid–structure interaction with multiphase viscous flows using an immersed body method. *Journal of Computational Physics*, 321:571–592.
- Yu, Q., H. Liu, T. Yang, and H. Liu. 2018. 3D numerical study on fracture process of concrete with different ITZ properties using X-ray computerized tomography. *International Journal of Solids and Structures*, 147, 204-222.
- Zhao, G.-F., A. R. Russell, X. Zhao, and N. Khalili. 2014. Strain rate dependency of uniaxial tensile strength in Gosford sandstone by the Distinct Lattice Spring Model with X-ray micro CT. *International Journal of Solids and Structures*, 51(7-8), 1587-1600.
- Zhao, Jiechao, and Guo Deyong, 2018, Cracking mechanism of coal under high-pressure water jet and its applications for enhanced coalbed methane drainage, *Arabian Journal of Geosciences* (2018) 11: 427



The SURE project has received funding from the European Union's Horizon 2020 research and innovation programme under grant agreement No 654662.

Zhu, J. B., T. Zhou, Z. Y. Liao, L. Sun, X. B. Li, and R. Chen. 2018. Replication of internal defects and investigation of mechanical and fracture behaviour of rock using 3D printing and 3D numerical methods in combination with X-ray computerized tomography. *International Journal of Rock Mechanics and Mining Sciences*, 106, 198-212.



The SURE project has received funding from the European Union's Horizon 2020 research and innovation programme under grant agreement No 654662.